

1 **Bedrock ledges, colluvial wedges, and ridgeline water towers:  
2 Characterizing geomorphic and atmospheric controls on the 2023  
3 Wrangell landslide to inform landslide assessment in Southeast  
4 Alaska, USA**

5  
6 Joshua J. Roering<sup>\*1</sup>, Margaret M. Darrow<sup>2</sup>, Annette I. Patton<sup>3</sup>, Aaron Jacobs<sup>4</sup>

7  
8 <sup>1</sup> Department of Earth Sciences, University of Oregon, Eugene, OR, USA

9 <sup>2</sup> Department of Civil, Geological, and Environmental Engineering, University of Alaska Fairbanks, Fairbanks, AK, USA

10 <sup>3</sup> College of Forestry, Oregon State University, Corvallis, OR, USA

11 <sup>4</sup> National Weather Service, Juneau, AK, USA

12 *Correspondence to:* Joshua J. Roering (jroering@uoregon.edu)

13 **Abstract.** In the past decade, several fatal landslides have impacted Southeast Alaska, highlighting the need to advance our  
14 understanding of regional geomorphic and atmospheric controls on triggering events and runout behaviour. A large and long  
15 runout landslide on Wrangell Island, with area in the top 0.5% of >14,760 slides mapped in the Tongass National Forest,  
16 initiated during an atmospheric river event in November 2023 and travelled >1 km downslope, causing six fatalities. We used  
17 field observations, sequential airborne lidar, geotechnical analyses, and climate data to characterize the geomorphic,  
18 hydrologic, and atmospheric conditions contributing to the landslide. Rainfall intensities recorded at the Wrangell airport were  
19 modest (~1-yr recurrence interval), but rapid snowmelt and drainage from a ridgeline wetland may have contributed to rapid  
20 saturation of the landslide. Although strong winds were recorded, we did not observe extensive windthrow, which may  
21 downgrade its contribution to slope failure. The landslide mobilized a steep, thick (>4 m) wedge of colluvium that accumulated  
22 below a resistant bedrock ledge and entrained additional colluvial deposits as it travelled downslope across cliff-bench  
23 topography. The substantial entrainment resulted in an unusually large width, extensive runout, and low depositional slope as  
24 the landslide terminated in the coastal environment. Our results suggest that the sequencing of rain- and snow-dominated  
25 storms, geologic controls on post-glacial colluvium production and accumulation, and ridgeline hydrology contributed to  
26 landslide initiation and mobility. Advances in post-glacial landscape evolution models, frequent lidar acquisition, and  
27 additional climate data are needed to inform regional landslide hazard assessment.

28 **1 Introduction**

29 In steep, forested landscapes, shallow landslides serve as the primary agent of erosion (Hovius et al., 1997; Korup et al., 2010;  
30 Larsen et al., 2010; Swanson et al., 1987), produce and transport sediment that contributes to aquatic habitat (Geertsema and  
31 Pojar, 2007), set the relief structure of mountain ranges (Stock and Dietrich, 2003), and constitute a significant hazard to

32 proximal communities and infrastructure (Godt et al., 2022). In contrast to bedrock landslides whose failures are governed by  
33 bedrock properties (Schuster and Highland, 2001; Wyllie and Mah, 2004), shallow landslides composed of loose,  
34 unconsolidated material tend to initiate in zones of thick colluvium that experience variable saturation due to precipitation and  
35 snowmelt and in turn generate debris flows or debris slides with significant downslope runout and inundation (Gabet and  
36 Mudd, 2006; Iverson, 2000). In unglaciated terrain, these shallow landslides often occur in unchannelled valleys (or hollows)  
37 at the upstream tips of valley networks that are subject to cycles of infilling and excavation over 10<sup>2</sup>- to 10<sup>4</sup>-yr timescales  
38 (Benda and Dunne, 1997; Dietrich et al., 1986; D'Odorico and Fagherazzi, 2003). Characteristic ridge-valley sequences in  
39 these settings have facilitated the identification and characterization of shallow landslide and debris flow processes and  
40 informed models for soil transport, near-surface hydrologic response, and landslide initiation and runout (Dietrich et al., 1995;  
41 Lancaster et al., 2003; Montgomery et al., 1997; Reid et al., 2016; Schmidt et al., 2001).

42 In contrast, in steep, post-glacial settings, terrain morphology tends to be dominated by glacial landforms and deposits such  
43 that dissection is patchy and weakly established (Brardinoni and Hassan, 2006). Specifically, shallow landslides tend to initiate  
44 within soils of thin-to-moderate thickness (1-3 m) on steep planar slopes and runout to valley floors or low-order channels that  
45 are often highly unstable and subject to frequent reorganization (Brardinoni et al., 2009). In these highly dynamic settings,  
46 topographic controls on colluvium accumulation along steep, unchannelled slopes is poorly constrained making it difficult to  
47 predict landslide entrainment and volumetric growth which largely determine runout and inundation (Brien et al., 2025; Iverson  
48 and Ouyang, 2015; Patton et al., 2022). Furthermore, the relative importance of processes that generate the accumulation of  
49 colluvium, such as in-situ weathering of till or bedrock, transport of soil or talus deposits, and deposition of allochthonous  
50 deposits (e.g., tephra), and thus promote initiation and entrainment is also poorly known (Bovy et al., 2016; Spinola et al.,  
51 2024). In these formerly glaciated hillslopes, the lack of a conceptual framework for the production and transport of  
52 unconsolidated material inhibits our ability to identify areas susceptible to shallow landsliding, runout, and inundation  
53 (Brardinoni et al., 2018; Guthrie, 2002).

54 The triggering of shallow landslides and debris flows in post-glacial terrain is primarily accomplished by storm events that  
55 generate intense rainfall over several hours (Fan et al., 2020; Guthrie et al., 2010; Patton et al., 2023; Swanston, 1969) and  
56 shallow subsurface stormflow that saturates colluvium and leads to elevated pore pressures. For example, Patton et al. (2023)  
57 used logistic regression and Bayesian methods to demonstrate that 3-hr rainfall intensity can effectively differentiate storms  
58 that trigger debris flows near Sitka, Alaska. Their analysis forms the basis of the *sitkalandslide.org* warning system that uses  
59 National Weather Service (NWS) forecasts to define the 3-hr rainfall intensity with medium (7 mm hr<sup>-1</sup>) and high (11 mm hr<sup>-1</sup>)  
60 levels of risk up to 3 days in the future (Lempert et al., 2023). Additional studies also highlight the importance of rain-on-  
61 snow events that can rapidly advect large quantities of water into near surface soil and bedrock and contribute to slope  
62 instability (Darrow et al., 2022). Field observations from recently failed head scarps reveal evidence for abundant seepage  
63 associated with permeability contrasts along the interface between bedrock, till, or colluvium as well as localized flow

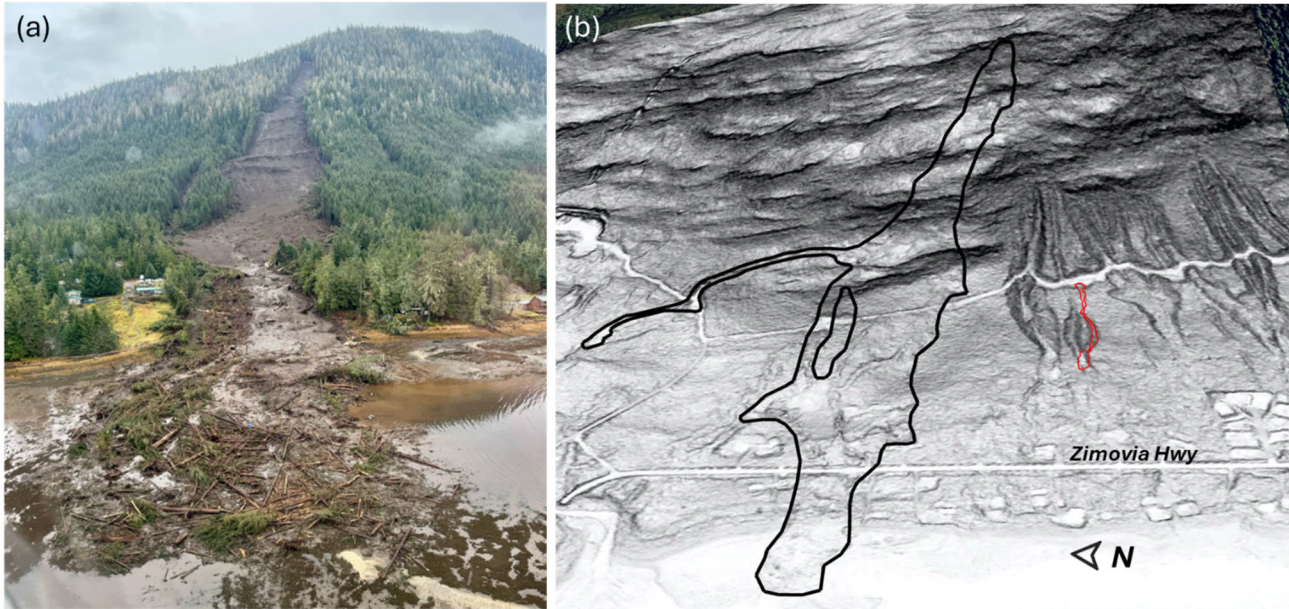
64 associated with fracture networks (Buma and Pawlik, 2021; Swanston, 1970). Notably, the upslope source of shallow  
65 groundwater and near-surface runoff that controls hydrologic response in post-glacial steeplands remains unclear owing to the  
66 paucity of high-resolution topography, field observations, and instrumental records in these settings. Additional factors  
67 contributing to landslide triggering in steep, forested terrain include timber harvest, fire, disease, and infestation, which can  
68 affect surface hydraulic properties and root reinforcement that resists sliding (Goetz et al., 2015; Johnson et al., 2000;  
69 Swanston, 1969). Extreme wind gusts have also been implicated in landslide initiation (Buma and Johnson, 2015; Lin et al.,  
70 2025; Parra et al., 2021) although the relative importance is difficult to determine and the mechanism by which wind gusts  
71 may contribute to slope failure is unclear and may include physical disturbance, progressive root failure, directed rainfall, or  
72 opening of hydrological pathways (Guthrie et al., 2010; Rulli et al., 2007). High winds can also contribute to rapid snowmelt  
73 (Hasebe and Kumekawa, 1995) and warm atmospheric rivers have been shown to promote snowmelt that substantially  
74 increases stream discharge (Guan et al., 2016; Hatchett, 2018; Henn et al., 2020).

75 The runout and inundation of landslides in post-glacial settings tends to be highly variable owing to variations in landscape  
76 dissection and the availability of unconsolidated material for entrainment. Most generally, the weakly-dissected slopes tend to  
77 generate fewer mobile slides that deposit on steeper slopes compared to slides in unglaciated settings (Booth et al., 2023;  
78 Vascik et al., 2021). Forest cover also affects landslide mobility, and the dense forest cover and large woody debris  
79 characteristic of many post-glacial settings favour lower mobility landslides (Booth et al., 2020). An abundance of datasets  
80 and models for the production and redistribution of colluvium that contribute to debris flow entrainment and volumetric growth  
81 have been generated in unglaciated settings (DiBiase et al., 2017; Gorr et al., 2022; Guilinger et al., 2023; Lamb et al., 2011;  
82 Reid et al., 2016; Rengers et al., 2020), but we lack both a framework and datasets that enable us to predict the runout, volume,  
83 and inundation of debris flows in post-glacial settings.

84 The need to improve our understanding of post-glacial shallow landslide triggers and processes in SE Alaska was highlighted  
85 by a large, catastrophic landslide that occurred on Wrangell Island on the evening of November 20, 2023. The landslide  
86 initiated during an intense rainfall event and entrained large quantities of colluvium and trees as it travelled downslope (Fig.1).  
87 Before terminating in Zimovia Strait, the landslide travelled over 1 km, inundated Zimovia Highway, destroyed three homes,  
88 and caused six fatalities (Nicolazzo et al., 2024), making it one of the deadliest landslides in Alaska history. This event was  
89 preceded and followed by several other fatal landslides in the region, including the 2015 Sitka, 2020 Haines, and 2024  
90 Ketchikan events. This concentration of activity motivates a detailed assessment of the geomorphic, geologic, and atmospheric  
91 factors contributing to the initiation and runout of impactful landslides in SE Alaska. Here, we use an array of tools to  
92 characterize the 2023 Wrangell landslide and describe how these findings will advance our ability to assess landslides in the  
93 region. In particular, our analysis addresses: 1) atmospheric processes, including precipitation and wind, that contributed to  
94 event triggering, 2) controls on the accumulation of unconsolidated material that promotes landslide initiation, downslope  
95 entrainment, and volumetric growth, 3) geologic and topographic controls on landslide runout and inundation, and 4) controls

96 on the organization and evolution of upslope drainage networks that modulate hydrologic response at the initiation zone. We  
97 leverage field observations, geotechnical measurements, sample analyses, climate data, change detection analysis from  
98 sequential airborne lidar data, an existing US Forest Service landslide inventory, and hydrologic flow routing analyses to assess  
99 the 2023 Wrangell landslide. Our findings provide critical information for identifying landslide triggers, mapping susceptible  
100 initiation zones, and modelling runout and inundation, and we propose specific steps, and research needs to advance landslide  
101 assessment in SE Alaska and other post-glacial landscapes to help reduce risk and minimize exposure during future events.

102



103 **Figure 1.** The November 20, 2023 MP11.2 Wrangell landslide: **(a)** Oblique aerial photograph facing east taken on November 22, 2023 by  
104 B. Salisbury (DGGGS), and **(b)** oblique lidar slopeshade image.

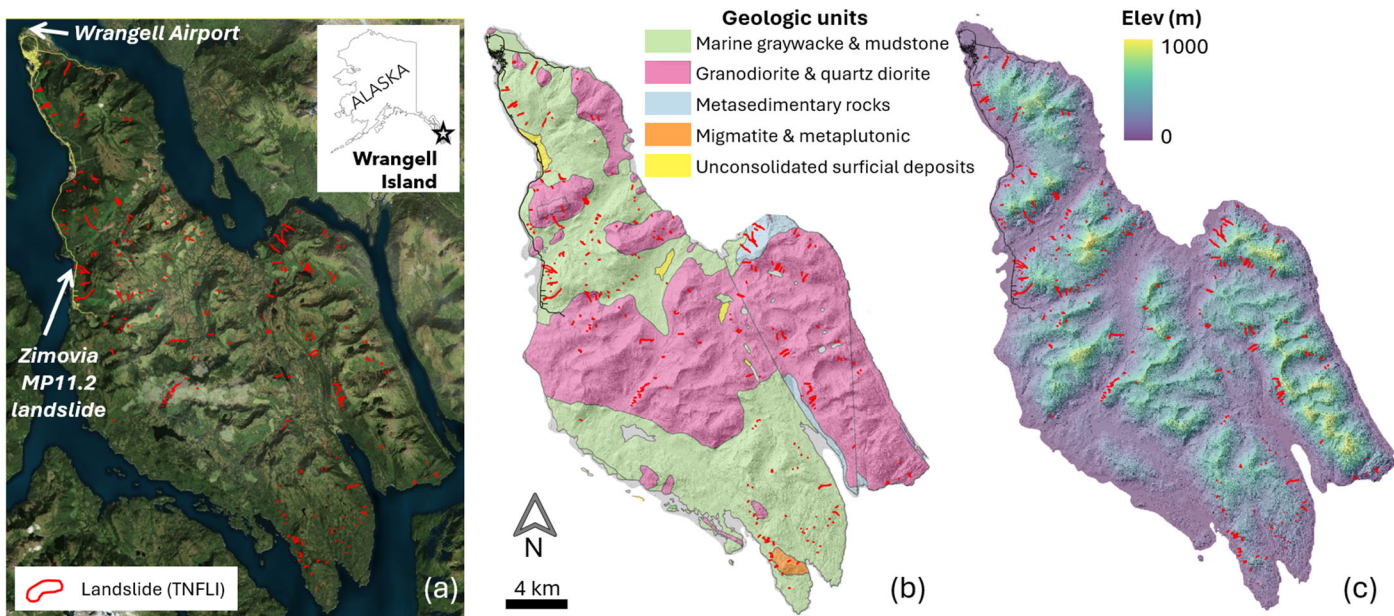
105 **2 Study site**

106 **2.1 Geology and geomorphology**

107 Situated in the southern half of southeast (SE) Alaska, Wrangell Island (Fig. 2) is composed of an assemblage of marine rocks  
108 in the Gravina coastal belt on the eastern margin of the Alexander Terrane that composes a substantial fraction of the region  
109 (Fig. 2b) (Haeussler, 1992; Wheeler and McFeely, 1991). Bedrock of the northern half of the island includes Cretaceous and  
110 Jurassic graywacke and Cretaceous intrusions (Karl et al., 1999). These turbidites and igneous rocks were deformed in the  
111 Late Cretaceous during the closing of a marine sedimentary basin between the Alexander terrane to the west and the Stikine  
112 terrane to the east (Haeussler, 1992). The graywacke is part of the Seymour Canal Formation, a unit with fine-grained,

113 rhythmically bedded turbidite deposits that are regionally recrystallized to slate or phyllite. The sandstone layers tend to be  
114 highly resistant and often form bedrock cliffs in areas with favourable dip direction.

115



116 **Figure 2.** Maps of Wrangell Island overlain with 256 landslide polygons (red) from the Tongass National Forest Landslide  
117 Inventory (TNFLI): (a) satellite imagery from Bing Satellite layer in QGIS Quick Map Services plug-in, (b) geologic units,  
118 and (c) lidar elevation and hillshade image.

119 The SE Alaska archipelago, including Wrangell Island, has been repeatedly glaciated, most recently during the Last Glacial  
120 Maximum, generating characteristic landforms, including cirques, uplifted shorelines, and broad U-shaped valleys (Fig. 2c)  
121 (Hamilton, 1994; Mann and Hamilton, 1995). By 13 to 15 kya, the margins of the Cordilleran Ice Sheet had retreated from SE  
122 Alaska fjords, channels, and interior passages, leaving isolated or stranded ice caps on some islands, with alpine or tidewater  
123 glaciers in many valleys and mountain peaks protruding above alpine glaciers (Carrara et al., 2003; Menounos et al., 2017).  
124 Broad and gentle uplifted shorelines (sometimes more than 100 m above sea level) with beach ridges, storm berms, and weak  
125 dissection, are abundant along coastlines in portions of SE Alaska (Baichtal et al., 2021) and may influence landslide runout.

126 On hillslopes, post-glacial landscape evolution is highly variable and some areas, particularly portions of western Wrangell  
127 Island, experience widespread slope modification from rockfall, talus accumulation, localized gullying, and landsliding.

## 128 **2.2 Climate and vegetation**

129 SE Alaska is a regional temperate rain forest with a maritime climate (Wendler et al., 2016). In Wrangell the mean annual  
130 precipitation is roughly 2 m, most of which falls as rain at low elevation with the proportion of rain-to-snow decreasing with  
131 elevation. In Wrangell and across SE Alaska, nearly all high-intensity rainstorms are associated with atmospheric rivers (ARs)  
132 (Nash et al., 2024), which are long (>2000 km), narrow (<500 km), moisture-laden currents in the lower troposphere (Neiman  
133 et al., 2008; Ralph et al., 2004). When ARs, which are most active August to November in SE Alaska, make landfall, orographic  
134 forcing can result in higher precipitation in mid-slope locations and on slope aspects that coincide with the trajectory of  
135 incoming ARs (Marra et al., 2022; Rulli et al., 2007). Although ARs account for only ~33% of annual precipitation, they  
136 generate 90% of extreme precipitation in the region (Sharma and Déry, 2020). As a result, ARs trigger the vast majority of  
137 shallow landslides along the Pacific coast of North America and SE Alaska (Cordeira et al., 2019; Oakley et al., 2018)

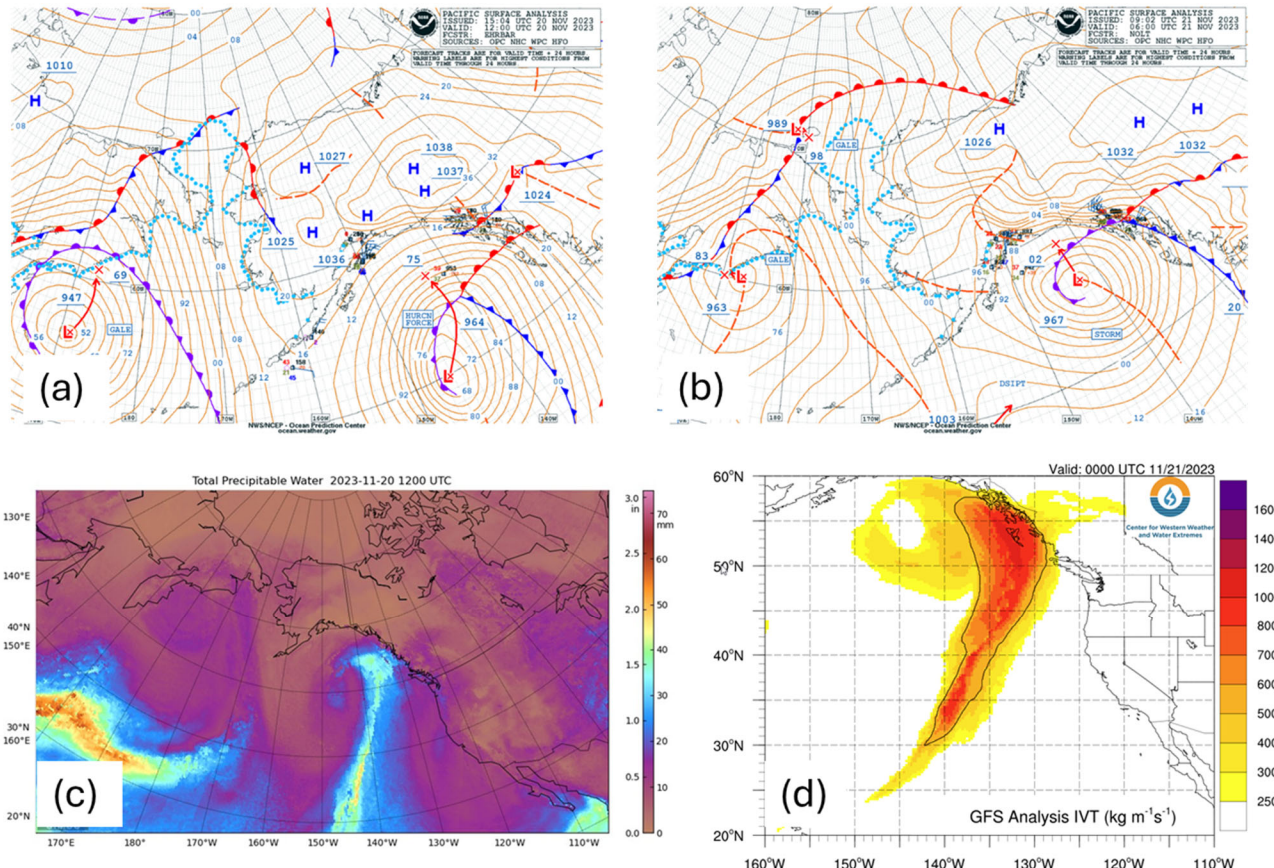
138 Much of SE Alaska is densely forested with mixed conifer forests of western hemlock (*Tsuga heterophylla*), Sitka spruce  
139 (*Picea sitchensis*), western red cedar (*Thuja plicata*), yellow cedar (*Callitropsis nootkatensis*), and mountain hemlock (*Tsuga*  
140 *mertensiana*) (Harris and Farr, 1974; Hees and Mead, 2005). Disturbed and riparian areas host locally abundant red alder and  
141 black cottonwood. Non-forested regions include high-elevation tundra vegetation and emergent wetlands (e.g., muskeg),  
142 surface water, glaciers, and snow/icefields (Flagstad et al., 2018). On Wrangell Island, logging since the 1950's along lower  
143 elevations has resulted in a mosaic of forest stand age. Although recent hemlock sawfly and western blackheaded budworm  
144 outbreaks have resulted in swaths of mid-elevation trees that have dropped their needles (Howe et al., 2024), the extent of tree  
145 mortality and impact on root systems, and thus slope stability, is not yet established.

## 146 **2.3 Landslides in Southeast Alaska**

147 Based on the Tongass National Forest Landslide Inventory (TNFLI), which includes >20,000 mapped slope failures and slide-  
148 prone areas (U.S. Forest Service, 2025b), the vast majority (>80%) of landslides in SE Alaska are debris flows or unchannelized  
149 debris avalanches that initiate within weathered till or colluvium during periods of intense rainfall (Fig 2a). The recent fatal  
150 landslides in SE Alaska were colluvial landslides, except for the 2020 Beach Road landslide in Haines that initiated within  
151 shallow bedrock during the December 2020 rain-on-snow event (Darrow et al., 2022). Extensive field-based research on  
152 landslide processes, particularly root reinforcement and hydrologic response, originated in the 1960s on Prince of Wales Island  
153 following increased landslide activity after timber harvest (Johnson et al., 2000; Swanston, 1969, 1970, 1973). These studies  
154 indicated that tree mortality affected landslide density as well as runout, such that landslides in harvested areas exhibited higher  
155 mobility (Booth et al., 2020; Buma and Johnson, 2015). The wide glacial valleys and weakly-dissected slopes in SE Alaska  
156 tend to favour infrequent landslide delivery to streams and most debris flow deposits contribute to fans or footslope deposits.

157 **2.4 The November 20, 2023 atmospheric river and impacts on Wrangell Island**

158 A hurricane-force 964 mb low pressure system lifted out of the North Pacific into the Gulf of Alaska during the early morning  
 159 hours of November 20, 2023 (Figure 3a). This low-pressure system proceeded along a north-northwest track, with the warm  
 160 front moving over southern and central SE Alaska before the front pushed north through the evening hours (Fig. 3b). A cold  
 161 air mass over northern SE Alaska and the Yukon produced a zone of high pressure and a strong pressure gradient across SE  
 162 Alaska. This colder air likely produced snowfall at higher elevations prior to the arrival of warm, moist air. This weather  
 163 system included significant subtropical moisture and additional AR characteristics evident in satellite imagery (Fig. 3c). At 3  
 164 PM on November 20, the CIMMS Model analysis of Integrated Water Vapor Transport (IVT), a commonly used indicator of  
 165 ARs, indicated very high IVT over the southern half of SE Alaska (Fig. 3d).

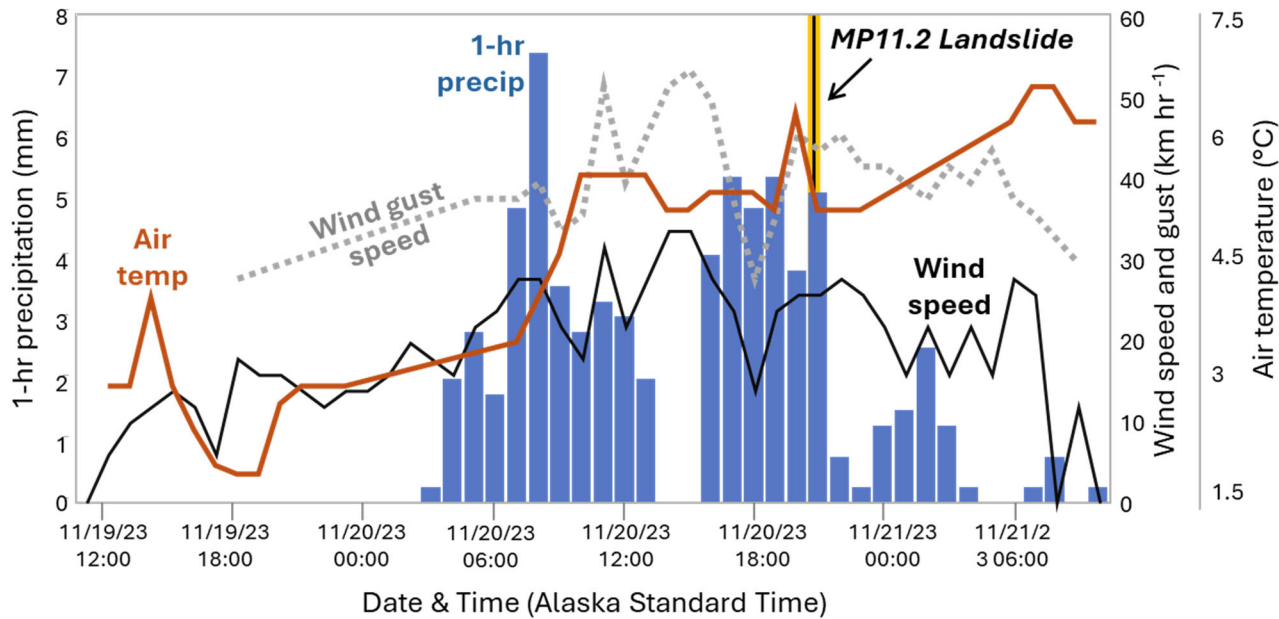


166 **Figure 3.** The November 20, 2023 atmospheric river event: (a) NOAA surface analysis from imagery from November 20 at  
 167 4am Alaska Standard Time, (b) NOAA surface analysis from imagery from November 20 at 10pm Alaska Standard Time, (c)  
 168 Total Precipitable Water from the Cooperative Institute for Meteorological Satellite Studies (CIMSS) Morphed Integrated

169 Microwave Total Precipitable Water (MIMIC-TPW) for November 20 at 4am Alaska Standard Time, **(d)** Integrated Water  
170 Vapor Transport (IVT) from Center for Western Weather and Water Extremes (C3WE) from November 20 at 4pm.

171

172 Heavy precipitation and high wind gusts began in the morning hours of November 20 and warm air and moisture combined  
173 with high winds likely melted snow at higher elevations. That afternoon, numerous landslides and road blockages were reported  
174 on Prince of Wales Island near Craig, Klawock, and Black Bear. The front shifted to an eastward trajectory in the early evening  
175 hours, as heavy rain and winds shifted towards Wrangell Island, and reports of the Zimovia Highway milepoint (MP) 11.2  
176 landslide were received just before 9 pm Alaska Standard Time. The front continued eastward, and rain and winds diminished  
177 through the night. The 24-hr precipitation totals on Prince of Wales varied from <5 cm to >16 cm on the east and west sides  
178 of the island, respectively (National Oceanographic and Atmospheric Administration (NOAA), 2024). At Wrangell airport,  
179 which is situated at sea level near the northern tip of the island and over 15 km north of the MP11.2 landslide (Fig. 2a), 8 cm  
180 of rainfall was recorded in 24 hours, and nearly half of that rainfall total was delivered steadily between 3 pm and 9 pm (Fig.  
181 4). Peak wind speed and gusts of 30 and 50 km hr<sup>-1</sup>, respectively, occurred from 11 am to 3 pm and sustained at high levels  
182 through the evening. Air temperature rose rapidly in the morning and remained above 5°C. A remote weather station located  
183 ~25 km west of the MP11.2 slide at 275m above sea level on Zarembo Island recorded similar wind speeds as the Wrangell  
184 airport but notably logged a short period of gusts >100 km hr<sup>-1</sup> around 7 pm in conjunction with a southward shift in direction  
185 of the front (Nicolazzo et al., 2024). Local observations during the day of the storm are notable because several residents  
186 reported: 1) rainfall to be more intense along Zimovia Highway than in Wrangell, and 2) significant snow cover at mid-to-high  
187 elevations prior to the November 20 storm that melted by November 21.



188 **Figure 4.** Time series of hourly climate data from Wrangell Airport spanning November 19 to 21, 2023, including: 1-hr  
 189 precipitation (blue bars), average wind speed and maximum wind gusts (black and dashed grey lines, respectively), and air  
 190 temperature (red line). The MP11.2 landslide occurred at ~9pm on November 20 (vertical yellow/black line).

191

192 On November 21, Alaska Governor Dunleavy issued a state disaster declaration, and the Alaska Division of Geological &  
 193 Geophysical Surveys (DGGS) was contracted to document landslides triggered on Wrangell Island during the storm. DGGS  
 194 used airborne lidar acquired in July and on November 28-29, 2023, to estimate the character and volume of the MP11.2 and  
 195 nearby landslides (Nicolazzo et al., 2024). For the MP11.2 landslide, they noted under 80,000 m<sup>3</sup> of erosion, thick soil  
 196 entrained along bedrock benches, and an abundance of soil and large woody debris (with a negligible amount of bedrock)  
 197 composing the deposit. Portions of the deposit had been removed before the post-event lidar acquisition and the deposit  
 198 travelled nearly 150 m into the ocean, such that a small but non-negligible fraction of the deposit was not captured with lidar  
 199 differencing.

200 **3 Methods**

201 **3.1 Overview**

202 To assess and quantify controls on the initiation and runout of the MP11.2 landslide, we performed a wide array of analyses  
 203 and generated observations from fieldwork, community events, airborne lidar, hydrologic modelling, weather data, and

204 geotechnical testing. We endeavoured to address community-generated queries, such as the potential role of wind as a  
205 triggering agent and mechanisms responsible for the anomalously large size of the landslide.

206 **3.2 Landslide geometry**

207 To contextualize the MP11.2 landslide, we analysed the landslides previously mapped on Wrangell Island included in the  
208 TNFLI (n=20,235) (U.S. Forest Service, 2025b). We excluded snow avalanche chutes, snow avalanche fields, and debris  
209 avalanche fields because these extensive features reflect landforms that accumulate over time rather than discrete landslide  
210 events. For the remaining landslides (n=14,670), we identified those occurring on Wrangell Island and quantified the area,  
211 mobility (defined as H/L, where H is elevation difference between the head scarp and deposit and L is landslide length, defined  
212 as the horizontal distance between the head scarp and deposit), and aspect ratio (defined as W/L, where W is average landslide  
213 width).

214 **3.3 Field observations, sampling, and analyses**

215 To document failure mechanisms and runout behaviour, we traversed the entire length of the landslide, observing evidence of  
216 entrainment and deposition, and mapping localized seepage in the head scarp area. We collected representative soil samples,  
217 from which we determined gravimetric water content (American Society for Testing Materials, 2017a); particle-size  
218 distribution, consisting of sieve analysis (American Society for Testing Materials, 2017b), sedimentation analysis (American  
219 Society for Testing Materials, 2021), and specific gravity testing (American Society for Testing Materials, 2014b); Atterberg  
220 limits (American Society for Testing Materials, 2017a), and organic content by loss on ignition (Alaska Department of  
221 Transportation and Public Facilities, 2023). We also collected two volumetric samples using a soil sampler with inner brass  
222 rings, from which we determined dry unit weight and volumetric water content. We classified samples using the Unified Soil  
223 Classification System (American Society for Testing Materials, 2017a). We also collected estimates of intact bedrock strength  
224 using two Rock Schmidt Rebound Hammers (N-type and L-type, with impact energies of 2.207 Nm and 0.735 Nm,  
225 respectively). We followed standard methods (American Society for Testing Materials, 2014a) with the exception that we did  
226 not use a grinding stone on the in-situ rock faces. We also collected slices (or “cookies”) of four trees entrained in the deposit  
227 to determine their ages and obtained 35 bedrock and/or joint surface orientation measurements for kinematic analysis. Finally,  
228 we ventured onto the ridgeline above the landslide to document the upslope accumulation area that contributes surface water  
229 flow to the head scarp region.

230 **3.4 Topographic analysis: change detection, morphology, and hydrologic modelling**

231 To quantify the pattern of erosion and deposition, and controls on colluvial deposits and their entrainment in the landslide, we  
232 used the July 2023 and November 2023 lidar for change detection and topographic analysis (Zechmann et al., 2023, 2024).  
233 Both datasets have 0.5-m pixel spacing, high bare earth point density (>5 pts m<sup>-2</sup>), and high accuracy (<10 cm error in bare  
234 and vegetated areas). We used QGIS for our analyses and mapped the landslide extent using high-resolution imagery acquired

235 by the Alaska Department of Transportation and Public Facilities (ADOT&PF) and the airborne lidar data. By comparing  
236 numerous stable features in both lidar datasets we determined systematic offset to be negligible (<3 cm). For change detection,  
237 we applied raster-based subtractions and created a point layer for the landslide pixels, which we attributed with slope, elevation,  
238 land surface change using the digital terrain model (DTM, i.e., bare earth data), and vegetation change using the digital surface  
239 model (DSM,i.e., first return data). We used the derived points and their attributes in three primary ways: 1) maps of DTM  
240 and DSM change across the landslide and surrounding terrain, 2) plots of swath (10-m wide) averaged profiles of elevation,  
241 slope, and DTM / DSM change along a longitudinal transect that spans the central axis of the primary landslide, and 3)  
242 construction of a comprehensive mass balance of DTM change (i.e., erosion and deposition) along a cross-sectional transect  
243 that spans the entire width of the landslide.

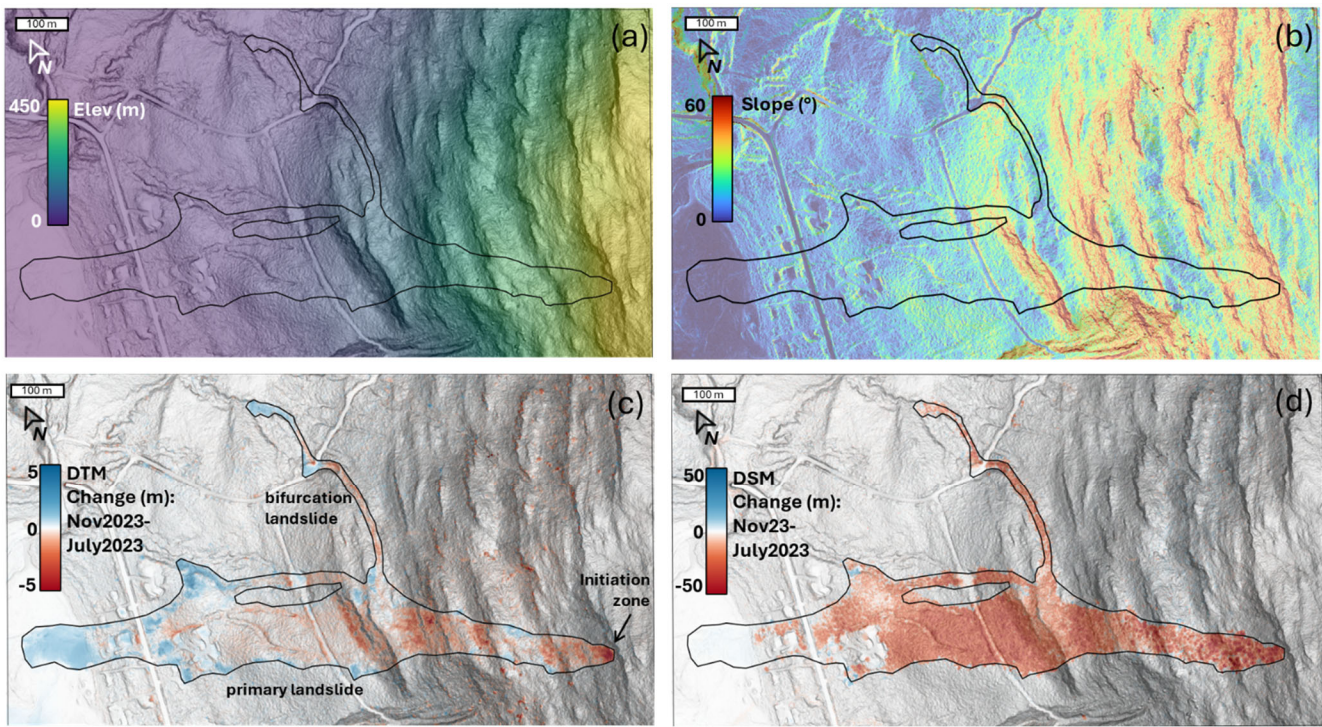
244 For the hydrologic modelling, we used TopoToolbox to define flow paths above the landslide scarp by removing sinks and  
245 defining flow directions and flow accumulation using a multiple flow direction (MFD) algorithm that partitions flow to all  
246 downslope pixels in proportion to the gradient of each pixel (Schwanghart and Scherler, 2014). In addition, we accessed the  
247 U.S. National Wetlands Inventory (Flagstad et al., 2018) in conjunction with our flow model to assess the potential contribution  
248 of wetlands to surface water flow and landslide triggering.

## 249 4 Results

### 250 4.1 Landslide geometry

251 The MP11.2 landslide has an area greater than 142,000 m<sup>2</sup> and initiated at 454m above sea level before flowing downslope  
252 >1km and depositing into the coastal marine environment (Fig. 5a). Although the width of the landslide averages 130 m, it is  
253 widest in the middle of the runout zone, and relatively narrow (<50m) at the initiation zone and terminus. Our analysis of  
254 landslides on Wrangell Island and in the TNFLI demonstrates that the MP11.2 landslide is notable for its areal extent (Fig.  
255 6a), which is more than twice the size of the next largest Wrangell Island landslide. When compared to the entire TNFLI, the  
256 MP11.2 landslide has a larger area than 99.5% of the landslides (Fig. 6b), which further demonstrates its exceptional size.

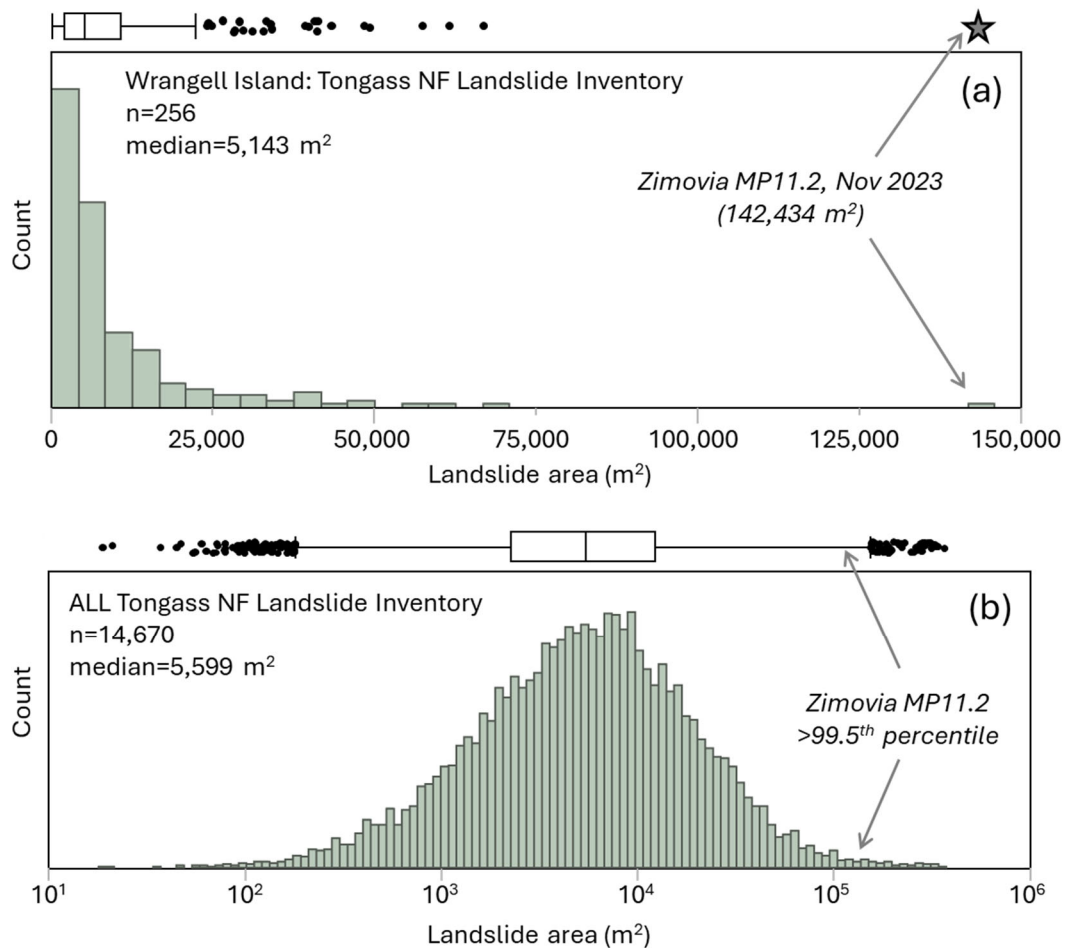
257 Given that landslide mobility (quantified as H/L, the value of which decreases with increased mobility) tends to vary with  
258 landslide size (Iverson et al., 2015; Rickenmann, 1999), we plotted H/L versus landslide area for the Wrangell Island landslides  
259 and fitted a logarithmic trend, such that H/L decreases slightly with area (Fig. 7a). In this context, the MP11.2 landslide is  
260 situated on the trend and thus does not appear notable for its mobility relative to its area. Because the MP11.2 landslide  
261 maintained a relatively wide footprint along most of its path, we also plotted W/L versus area (Fig. 7b) and noted a robust  
262 power-law trend indicating that slides tend to become increasingly elongate as they get bigger. In this context, the MP11.2  
263 landslide is anomalous for its large W/L value relative to its area. Specifically, the landslide plots well above the trend and  
264 only one of the 25 next largest landslides has a similar positive deviation above the area-W/L curve (Fig. 7b). In summary, the  
265 landslide did not appear to exhibit uncommon mobility as defined by H/L values, but rather it attained a large area while also  
266 maintaining substantial width, which contributed to its extensive inundation area and devastating impact.



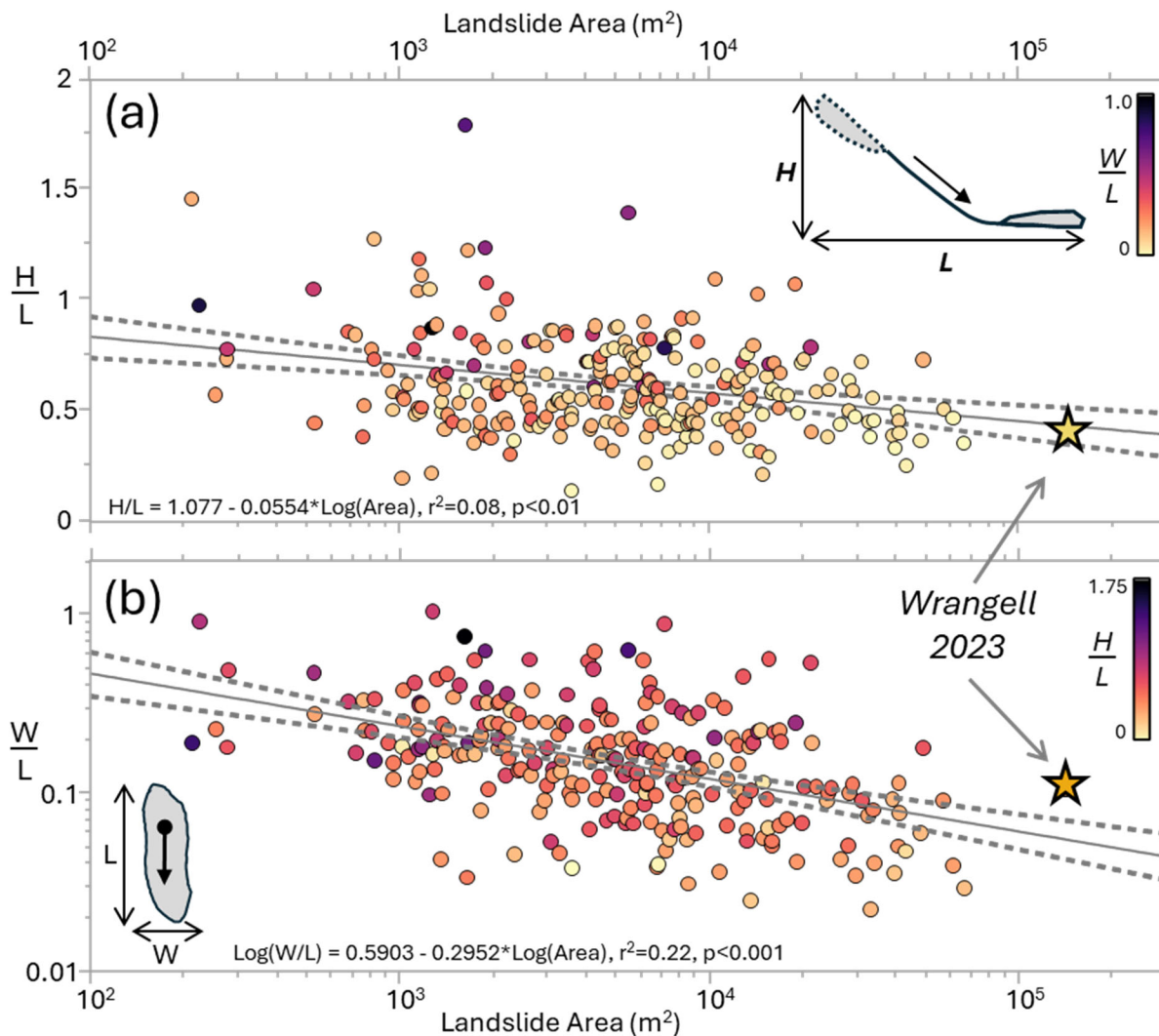
268 **Figure 5.** Lidar-derived maps of the MP11.2 landslide: (a) elevation above sea level in meters, (b) slope in degrees, (c) DTM  
 269 change (land surface or bare earth), and (d) DSM change (first return or canopy) with November 2023 dataset subtracted from  
 270 the July 2023 dataset such that negative values (red) reflect decreases and positive values (blue) reflect increases.

271

272



273 **Figure 6.** Histograms of landslide area from the TNFLI for (a) Wrangell Island and (b) all of the TNFLI, note the log scale.  
 274 The box-whisker plots above each histogram convey the median, interquartile range and outliers and the star denotes the  
 275 MP11.2 landslide.

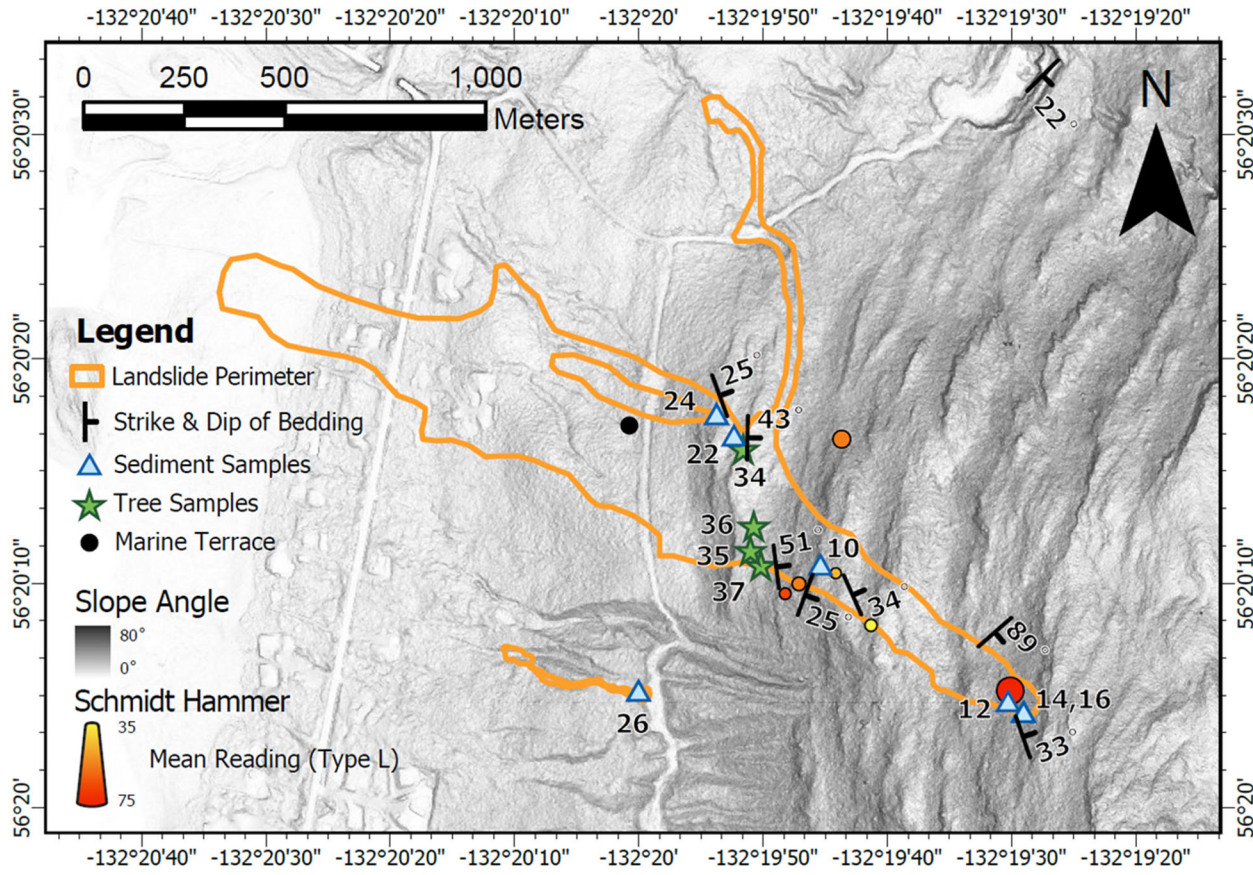


276 **Figure 7.** Plots of landslide characteristics for Wrangell landslides in the TNFLI. **(a)** Variation of mobility ( $H/L$ ) with area,  
277 and **(b)** variation of landslide aspect ratio with area. Note that the star indicates the MP 11.2 landslide in a and b. The solid  
278 black and dashed grey lines denote the regression fits and 95% confidence intervals for the equations indicated in a and b.  
279 Individual points are coloured by  $W/L$  in a and  $H/L$  in b.

280 **4.2 Geologic units, bedrock structure, and soil properties**

281 Marine sedimentary rocks of the Seymour Canal Formation (Karl et al., 1999) are exposed in the landslide and a bedrock  
282 quarry approximately 1.5 km north of the landslide head scarp (NE corner of map in Fig. 8). Bedrock lithology includes  
283 interbedded shale and graywacke typical of turbidite sequences with bedding dipping into the hillslope (to the east) within the  
284 landslide (Fig. 8). Local metasedimentary rocks on nearby hillslopes (slate and minor phyllite) indicate low-grade

285 metamorphism in the study area. Graywacke beds are 0.25- to 5-m thick as observed in the field and form benchlike  
 286 topography, with the resistant graywacke creating subvertical cliff bands within the landslide margin and across undisturbed  
 287 hillslopes, and the relatively weak shale forming low-gradient slopes (Fig. 5b). Bedding orientation in the quarry dips to the  
 288 southeast, indicating hillslope-scale folding (Fig. 8). In addition to bedding geometry, we documented three joint sets to assess  
 289 the potential for rock slope instability along the resistant bedrock cliffs. Preliminary kinematic analysis of discontinuities using  
 290 conservative friction angle estimates of 15° and 30° for shale and sandstone, respectively (Gonzalez de Vallejo and Ferrer,  
 291 2011), indicates that flexural toppling is possible while other rock failure mechanisms (direct toppling, wedge and planar  
 292 failure) are unlikely (supplemental materials).



293  
 294 **Figure 8.** Lidar hillshade map of MP11.2 landslide showing locations of field measurements and samples acquired during the  
 295 August 2024 field campaign. Strike and dip and Schmidt Hammer values denote averages within each sample locale.  
 296  
 297 We collected a total of 60 readings with each of the Schmidt Hammers. Using a correlation for sandstone, siltstone, and  
 298 mudstone that does not require rock density and uses the L-type hammer (Aydin and Basu, 2005), our estimates of uniaxial

299 compressive strength (UCS) average 90 MPa for measurements taken outside the lateral margins of the landslide body, 82  
300 MPa for measurements in the middle of the landslide body, and 148 MPa for measurements taken on massive greywacke  
301 exposed in the head scarp (supplemental materials). These values are typical for graywacke (Gonzalez de Vallejo and Ferrer,  
302 2011) and indicate that the estimated UCS of the exposed graywacke in the head scarp is 80% higher than that within the lower  
303 landslide body and 64% higher than bedrock exposures adjacent to the MP11.2 landslide.

304 In exposures along the landslide flanks, we observed colluvium as discontinuous “wedges” at the base of bedrock cliffs,  
305 including a ~4 m thick deposit that constitutes the initiation zone (Fig. 9a). The matrix of the colluvium was brown, organic  
306 silty sand to silty sand with gravel (SM), similar to displaced landslide material observed downslope. The material properties  
307 of the colluvium imply moderate frictional strength, minimal weathering or alteration, and relatively high permeability. All of  
308 the samples tested were non-plastic (supplementary materials). In an area scoured by the landslide in its depositional zone, we  
309 also observed a deposit of sand and subrounded, imbricated gravel characteristic of coastal marine sediments. The deposit is  
310 exposed just below the USFS road at approximately 100 m elevation, which is consistent with estimated glacial isostatic  
311 adjustment documented for the region (Baichtal et al., 2021).

312



313 **Figure 9.** Photographs of key features identified in the field: (a) view to the north across the head scarp, exposing thick (~4m)  
 314 colluvial wedge in lateral margin, (b) ridgeline wetland or muskeg that drains to the head scarp, and (c) oblique view of mid-  
 315 slope location (~1,000 m on transect; see Fig. 11) depicting high relief and resistant cliff-forming unit and patch of live  
 316 blueberry bushes just below the top of the bedrock cliff. Note person for scale.

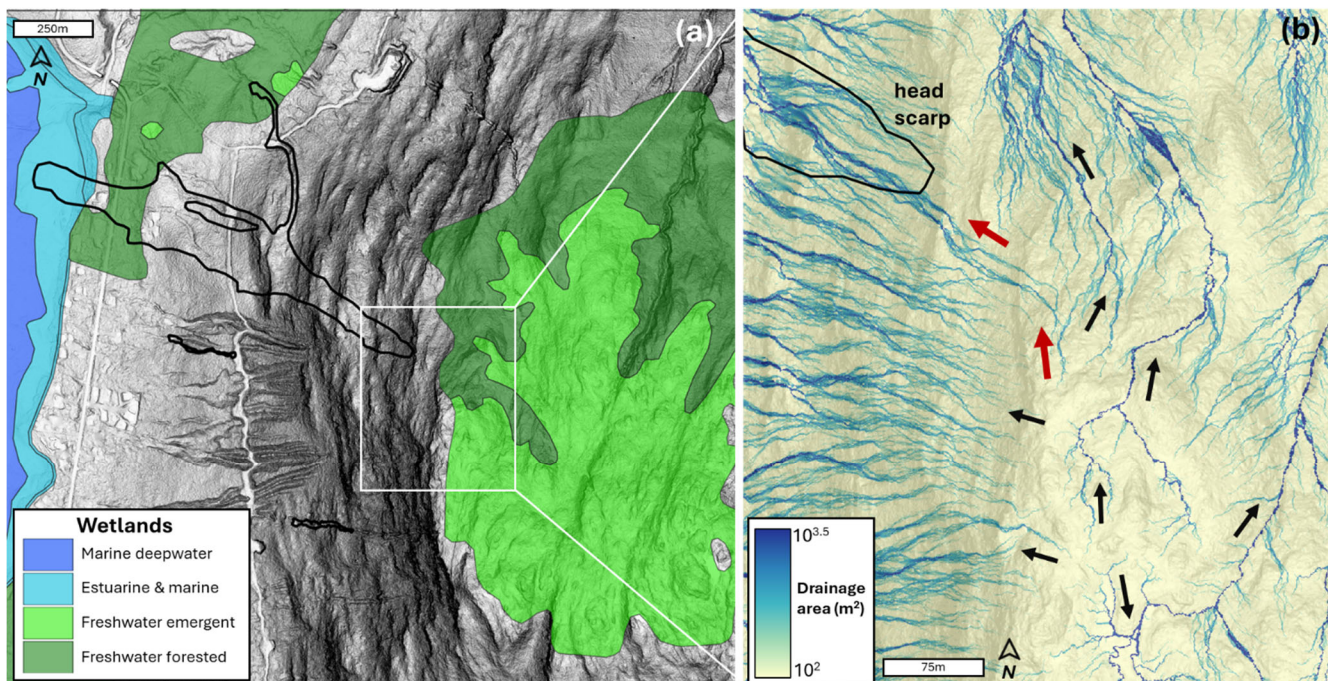
317 **4.3 Landslide initiation and triggering factors**

318 The initiation zone for the MP11.2 landslide has an average slope of  $42\pm2.5^\circ$  and is approximately 30-m wide and 26-m long  
 319 (Fig. 5b, d). According to lidar differencing of the pre- and post-event DTMs, the average thickness of the initiation zone is  
 320  $4.5\pm0.7$  m (Fig. 5c), which is thick relative to many landslides observed in the Tongass National Forest. In the days following  
 321 the landslide, aerial imagery acquired by the Alaska Department of Transportation and Public Facilities (ADOT&PF) revealed  
 322 prodigious seepage emanating from the SE corner of the head scarp, and during our August 2024 field campaign we noted  
 323 localized seepage in that location despite negligible rainfall in the preceding days. Additional triggering factors include

324 compromised root reinforcement, and we noted an abundance of standing Western hemlock trees without needles just beyond  
325 the northern and southern margins of the initiation zone.

326 In the 6 hours prior to the MP11.2 landslide, rainfall intensity at the airport averaged  $5 \text{ mm hr}^{-1}$  (Fig. 4), which corresponds to  
327 a  $\sim 1$ -yr return interval (National Oceanographic and Atmospheric Administration (NOAA), 2024). In addition, the maximum  
328 3-hr intensity just prior to the slope failure was less than the  $7 \text{ mm hr}^{-1}$  intensity threshold that delineates an elevated level of  
329 risk in the Sitka region. Notably, high winds and warm temperatures characterized the 12-hour period prior to the landslide,  
330 and these changes may have contributed to the failure through mechanical disturbance and rapid delivery of snowmelt to the  
331 initiation zone. Observational records of these potential triggering factors proximal to the landslide are lacking, so we explored  
332 alternative sources of evidence. To assess the potential role of wind disturbance in landslide triggering we used differencing  
333 of the canopy (or DSM) lidar data to map wind throw (or tree turnover) as a signature of canopy disturbance proximal to the  
334 initiation zone (Fig. 5d). Consistent with our field observations, our map of DSM change does not reveal evidence for  
335 widespread canopy disturbance beyond the margins of the landslide. In fact, the DSM change map revealed less than 10  
336 individual and localized tree turnover events dispersed within several kilometres of the MP11.2 landslide.

337



338 **Figure 10.** Lidar maps of MP11.2 landslide and relevant drainage features. (a) Shaded relief image of landslide and extent of  
339 ridgeline wetland from the National Wetlands Inventory, (b) map of contributing drainage area along the ridgeline above the  
340 MP11.2 landslide. Note the radial flow pattern that includes a significant area flowing to the head scarp (red arrows).

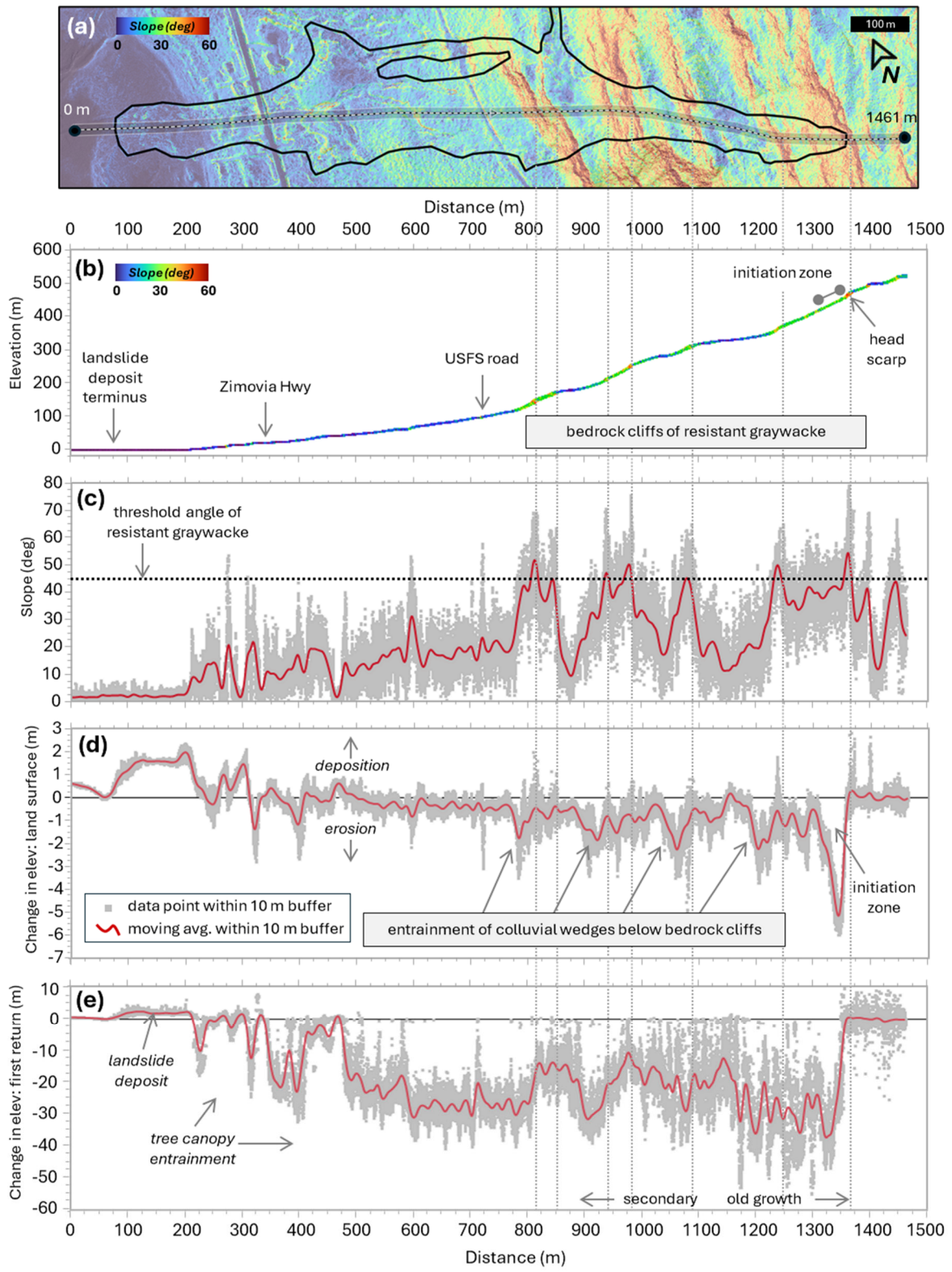
341

342 To assess the potential contribution from ridgeline wetlands and rapid snowmelt on the saturation of the initiation zone, we  
343 mapped wetlands and hydrological flow paths upslope of the head scarp (Fig. 10a). Our map shows a radial drainage pattern  
344 emanating from the ridgeline with an array of dispersed, west-directed flowpaths that drain to slide-prone slopes to the south  
345 of the MP11.2 landslide (Fig. 10b). By contrast, flowpaths oriented to the north, east, and south tend to exhibit an incised and  
346 well-defined channel network structure that is reflected by the narrow, dark blue (high drainage area) tendrils that contrast  
347 with the more diffusive flowpaths with wider and lighter blue (lower drainage area) signatures draining west (Fig. 10b). This  
348 pattern likely reflects the relative antiquity of channels and flowpaths draining from the ridgeline to the north, east, and south.  
349 Notably, an elongate system of flowpaths is situated between the west- and north-directed drainages. This flow accumulation  
350 pathway denoted by red arrows in Fig. 10b demarcates a substantial drainage area directed to the SE corner of the MP11.2  
351 landslide head scarp and coincident with abundant seepage observed in the field. Our flow mapping indicates greater than  
352 6,000 m<sup>2</sup> of drainage area upslope of the head scarp, and this source area includes a substantial fraction of low-gradient,  
353 emergent wetlands with patchy bedrock exposure (Fig. 9b, 10a). In the field, this ridgeline wetland area (muskeg) was  
354 characterized by deep (>2 m), organic soil akin to peatlands. Curiously, the flowpaths that contribute to the landslide head  
355 scarp also reveal evidence of bifurcation into slide- and north-directed drainage systems (Fig. 10b). Our field observations  
356 indicate that this bifurcation corresponds to meter-scale roughness in the bedrock/wetland surface, implying that the orientation  
357 of ridgeline drainage may be highly dynamic and sensitive to local disturbances.

#### 358 **4.4 Landslide runout and mass balance**

359 Our lidar and field analyses reveal strong topographic and geologic controls on the pattern of erosion and deposition along the  
360 landslide runout path (Fig. 11). These analyses focus on the primary landslide path and do not include the north-directed  
361 bifurcation that occurred in the middle sections and accounted for a small fraction of the slide volume. Our field observations  
362 indicate that the initiation zone was localized to the upper 30 m (~1350 m on our transect; Fig. 11a) such that runout processes  
363 are responsible for the downslope pattern of erosion and deposition. The W-NW directed path of the slide does not exhibit  
364 topographic convergence as expressed by contour (or planform) curvature and thus lateral confinement did not affect the runout  
365 behaviour. Rather, our 10-m wide swath-averaged transect data show that the lower half of the ~1,250-m long runout is  
366 characterized by a low-gradient surface with slope angles that seldom exceed 20° (Fig. 11a-c). This zone of relatively gentle  
367 topography coincides with our observations of nearshore/coastal deposits found at approximately 100 m above sea level. In  
368 contrast, the upper half of the runout zone (between 800 and 1300 m along our transect) is characterized by a sequence of 5 to  
369 7 step-bench segments (Fig. 11c). Steep cliffs of exposed bedrock are defined by east-dipping resistant graywacke beds that  
370 manifest as continuous ledges across the landscape (Fig. 1). The intervening low-gradient (<20°) benches tend to be broad and  
371 approximate bedding planes with a carapace of locally derived colluvium. These steps composed of cliff-bench sequences are  
372 ubiquitous in the marine sedimentary units across Wrangell Island and they are associated with numerous long-runout  
373 landslides in the TNFLI.

374



376 **Figure 11.** Analysis of landslide properties along a 10-m wide longitudinal transect of the MP11.2 landslide. (a) Lidar map of  
377 slope angle overlain on shaded relief map with transect location and endpoint distances depicted, (b) lidar-derived elevation  
378 values from the November 2023 acquisition with points coloured by slope angle in degrees, (c) lidar-derived slope angle, (d)  
379 DTM (or land surface) change, and (e) DSM (or canopy) change for all points within 10 meters of the transect (grey points)  
380 and running average (red line).

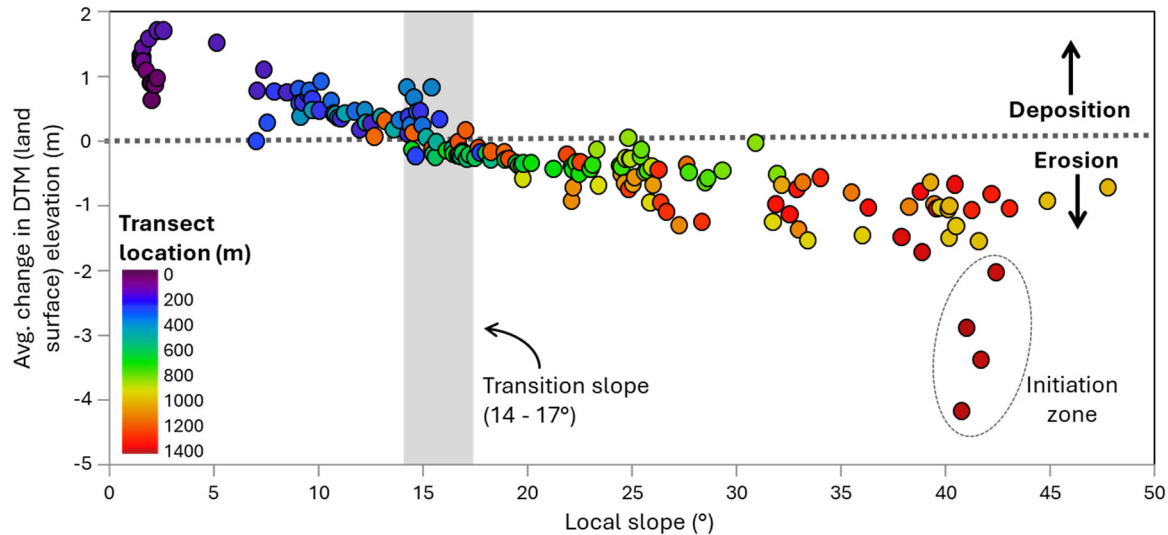
381

382 Our profile of DTM (or land surface) change shows that net erosion tends to dominate in the upper half of the landslide while  
383 negligible net surface change and deposition characterize the lower half (Fig. 11d). The pattern of erosion in the upper half is  
384 strongly correlated with the cliff-bench sequences. Specifically, local erosion maxima of 1 to 2 m (denoted by negative values  
385 of surface change) span 25 to 50 m horizontally and occur just downslope of the steep bedrock cliffs where they transition to  
386 the low-gradient benches (Fig. 11d). These foci of erosion coincide with field observations of colluvial wedges exposed along  
387 the lateral margins of the landslide. Our analysis reveals minimal erosion along the low-gradient benches that are situated  
388 below these colluvial wedges, and in the field these benches exhibited patchy entrainment as well as minor local deposition.  
389 In the field, we also observed a live blueberry patch growing on a subvertical bedrock face at ~1000 m along the transect (Fig.  
390 9c, 11c). This observation implies negligible erosion, and perhaps projectile behaviour of the landslide runout.

391 The profile of DSM (or canopy) change indicates removal of trees taller than 50 m in the upper 200 m of the initiation and  
392 runout zones, whereas trees less than 40 m in height were mobilized from the lower area of the landslide (Fig. 11e). This  
393 pattern results from pre-1965 timber harvests along the lower slopes in our study area with the transition to unmanaged forest  
394 at 1,100 m along our transect (Fig. 11e). We sampled cookies from four western hemlock trees transported by the landslide  
395 and deposited along the slide margins at approximately 900 m along our transect. The violent nature of the landslide snapped  
396 the tree trunks, and we estimated that the lower 3 to 5 m of each trunk was missing. To account for the missing record, we  
397 added 20 years to the age of each tree. The four trees ranged from  $292 \pm 10$  to  $322 \pm 10$  years old, indicating that they originated  
398 from the old growth towards the top of the landslide. We also noted that reaction wood (which can be indicative of slope  
399 movement) was present in all tree samples.

400 We plotted average surface or DTM change against local slope for 10-m intervals along the transect to assess mechanical  
401 controls on debris flow entrainment and deposition (Fig. 12). Net erosion dominates when local slope exceeds  $15^\circ$  and the  
402 average value of net erosion increases with slope from  $15^\circ$  to  $45^\circ$ . Notably, points defining this trend occur at a wide range of  
403 locations along the transect, reflecting the profound influence of local slope on debris entrainment. That said, locations along  
404 the middle section of the landslide, which are denoted by filled green circles (Fig. 12), tend to have lower values of net erosion  
405 compared to upslope locations, which may result from variations in debris availability and saturation or changing inertial forces  
406 that control entrainment. For slopes between  $41^\circ$  and  $44^\circ$ , we observed several values of high net erosion ( $>2$  m) that deviate  
407 from the local slope-erosion trend. These values (denoted by dark red filled circles and a dashed ellipse in Fig. 12) occur at the  
408 uppermost extent of the landslide and are associated with the initiation zone and thus reflect mechanical processes that differ  
409 from downslope areas that experienced entrainment. For slope angles less than  $15^\circ$  we observe a trend of increasing deposition

410 with decreasing slope and a clustering of 0.7 to 1.7 m of deposition at  $2^\circ$  that defines the landslide toe. These trends define the  
 411 slope-dependent transition between erosion and deposition for runout models, as well as provide constraints on entrainment  
 412 potential.

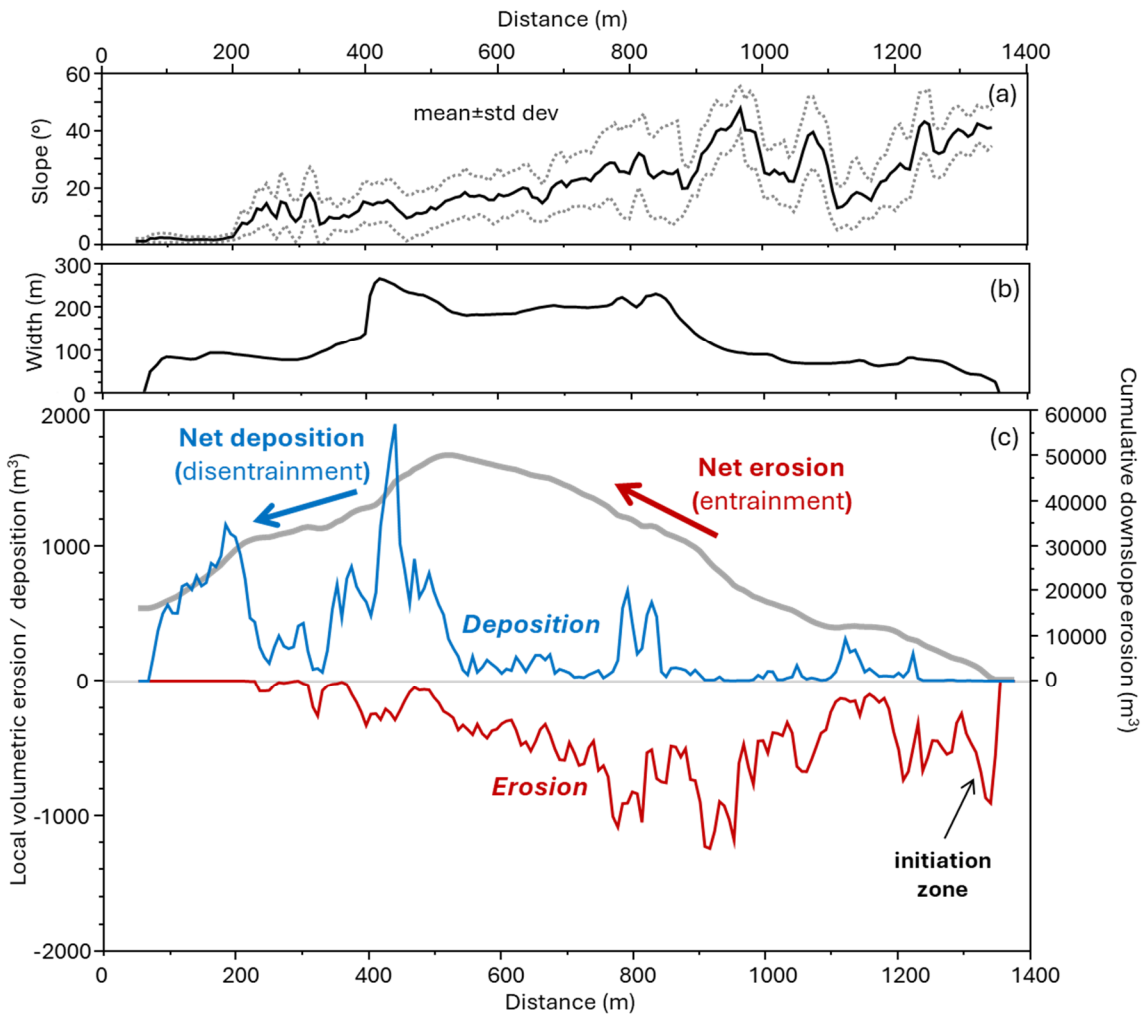


413 **Figure 12.** Variation in local net erosion and deposition with slope angle. Values are averaged for 10-m bins along the transect  
 414 in Fig. 11a. Colours reflect distance along the transect and the vertical grey rectangle denotes the transition slope between  
 415 erosion and deposition. The dark red points enclosed by a dashed ellipse denote the initiation zone.

416

417 We performed a mass balance of erosion and deposition along the MP11.2 landslide to identify the downslope transition of  
 418 net erosion to deposition and quantify the total volume of erosion and deposition associated with the landslide (Fig. 13).  
 419 Specifically, we tallied the total thickness of both erosion and deposition for all points within the landslide boundary using 10-  
 420 m wide swaths oriented perpendicular to the longitudinal transect (Fig. 11a) and then separately summed the values within  
 421 each swath. The distance between distal points along this transect defines the width of the landslide, which averaged less than  
 422 100 m in the upper 500 m of the slide, increased abruptly to greater than 200 m through the middle section, and then decreased  
 423 to  $\sim 100$  m in the lower depositional zone (Fig. 13b). Our mass balance analysis indicates high erosion at the initiation zone  
 424 that decreased downslope before increasing rapidly just above the middle section, which coincides with landslide widening  
 425 (red line in Fig. 13c). In the lower portions of the wide zone (400 to 500 m along the transect), we observe an abrupt transition  
 426 from erosion (red line) to deposition (blue line) with a depositional peak that corresponds to the widest section of the landslide.  
 427 In the field, this zone of localized widening corresponded with extensive accumulation of downed trees on the north flank of  
 428 the landslide. Substantial deposition is associated with the landslide deposit (located between 75 and 250 m along the transect),  
 429 just below a zone of local steepness (250 to 350 m along the transect) that experienced efficient transport and minimal  
 430 deposition or erosion.

431



432 **Figure 13.** Downslope mass balance analysis of the MP11.2 landslide. Profiles of (a) slope, (b) width, and (c) local erosion  
 433 (red), local deposition (blue), and cumulative erosion minus deposition (gray curve) calculated for all points within the  
 434 landslide boundaries along the transect in Fig. 11a. Note that the northward bifurcation pathway (Fig. 5a) is not included in  
 435 this analysis.

436

437 Lastly, we integrated total erosion and deposition along the landslide path by starting at the head scarp and summing the  
 438 imbalance in erosion (positive values of erosion) and deposition (negative values of erosion) in the downslope direction (see  
 439 grey curve in Fig. 13c), finishing at the slide terminus. Cumulative erosion increases monotonically in the downslope direction  
 440 before peaking at ~550 m along the transect. This implies an average volumetric growth factor of  $62 m^3 m^{-1}$  along the erosional  
 441 portion of the landslide, although local variations associated with changes in slope occur. Downslope of the net erosion peak,  
 442 the slide widened and the slope became gentler, and as a result deposition outpaced erosion downslope. At the slide terminus,

443 the erosion-deposition balance did not approximate zero, however, indicating that net erosion exceeded deposition. In total,  
444 we estimated 65,300 m<sup>3</sup> of erosion and 49,400 m<sup>3</sup> of deposition for the primary landslide, which implies an imbalance of  
445 >15,000 m<sup>3</sup> that may reflect debris loss in the coastal deposition zone as well as detection limits in depositional areas and  
446 changes in bulk density. For the mass balance of the north-directed bifurcated portion of the landslide (Fig. 5c), we observed  
447 4,000 m<sup>3</sup> of erosion and 3,800 m<sup>3</sup> of deposition.

448 **5 Discussion**

449 **5.1 Initiation and triggering factors**

450 Our preliminary investigation indicates that the MP11.2 landslide was an anomalously large and thus long-runout event that  
451 initiated in a steep and wide deposit of thick colluvium during a notable but not atypical SE Alaska storm event. A wide range  
452 of factors may have affected the initiation of the landslide and the uncertainty ascribed to our interpretations reflects limitations  
453 in data availability, chiefly local climate observations, to test landslide initiation hypotheses. By contrast, geomorphic and  
454 geologic factors that predisposed the hillslope to landsliding are more straightforward and provide important considerations  
455 for the assessment of landslide hazard and risk in other locations.

456 Initiation of the MP11.2 landslide likely required a high degree of soil saturation to overcome the shear strength of the  
457 colluvium and promote the observed highly mobile, fluid-like runout. The rainfall intensity that preceded the landslide was  
458 notable but not extraordinary, as quantified by the 1-yr recurrence interval and 3-hr and 6-hr intensities recorded at Wrangell  
459 airport. Given the 15-kilometer distance between the airport rain gauge and the landslide, and the greater than 400 m elevation  
460 of the initiation zone, the rainfall experienced at MP11.2 is highly uncertain. During our community events, several residents  
461 that drove along the Zimovia Highway on November 20 noted that rainfall south of Wrangell and closer to the landslide area  
462 was more intense than in the town. In addition, several residents reported the presence of a substantial snowpack at mid- and  
463 upper slope locations on the morning of November 20. At the airport weather station at sea level, air temperatures were cold  
464 (~2°C) on November 19 and warmed rapidly on the morning of November 20, coincident with the arrival of abundant rainfall.  
465 The temporal trend in air temperature at the initiation zone and ridgeline was likely similar although the absolute temperatures  
466 were likely lower owing to the higher elevation. As a result, the rapid warming on November 20 combined with hours of  
467 moderate-intensity rainfall may have generated substantial runoff via snowmelt. Days after a snow-dominated atmospheric  
468 river, an extreme rain-dominated (1 in 500 yr event) atmospheric river generated widespread landslides and the fatal Beach  
469 Road landslide in nearby Haines, AK, in December 2020. The scale and impact of these recent events suggest that the  
470 sequencing and pacing of snow- and rain-dominated storms may be a critical factor in landslide initiation in SE Alaska. As  
471 such, monitoring rain and snow in a wide range of settings is crucial for advancing our understanding of the hydrologic  
472 response that contributes to landsliding.

473 The potential of high wind as a driver of recent landslides across SE Alaska, including the MP11.2 event, has been surmised  
474 by many residents. Tree turnover (or windthrow) can contribute to the initiation of shallow landslides and debris flows based

475 on observations from extreme storms (Guthrie et al., 2010; Lin et al., 2025). Such events tend to trigger widespread windthrow,  
476 however, which was not observed on Wrangell Island during the November 20 storm. In the absence of tree turnover, the  
477 potential for trees to transmit dynamic forces into the subsurface due to high winds has not been well-studied. Alternatively,  
478 windthrow may impact slope stability through the reduction of root reinforcement (Parra et al., 2021). Pioneering research  
479 documenting timber harvest impacts on slope stability was performed in SE Alaska on nearby Prince of Wales Island (Wu et  
480 al., 1979) and those studies demonstrated the substantial contribution of soil shear strength through root reinforcement. More  
481 recent advances highlight how the progressive tensile loading of root systems in shallow soils undergoing shear can be  
482 quantified to assess slope stability in three dimensions, which is critical for capturing how roots reinforce the lateral margins  
483 of potentially unstable slopes (Cohen et al., 2009). These studies demonstrate that as soils get thicker, the relative contribution  
484 of root reinforcement to the total shear strength decreases substantially given that root density decreases exponentially with  
485 depth (Schmidt et al., 2001). The root systems of coniferous forests tend to be concentrated in the upper 1 m (Hales, 2018;  
486 Jackson et al., 1996) and as a result, root reinforcement was likely a minor contributor to the cumulative shear resistance of  
487 the nearly 5-m thick initiation zone of the MP11.2 landslide. Nonetheless, the contribution may not be negligible, and further  
488 analysis of the potential impact of the abating sawfly and budworm infestations on the root systems of western hemlock and  
489 Sitka spruce trees in SE Alaska warrants further investigation. The infestation resulted in moderate-to-severe (11-50%)  
490 mortality of infested trees on Wrangell Island and impacts are common on west-facing slopes and at elevations that coincide  
491 with the initiation zone (U.S. Forest Service, 2025a).

492 Windy conditions can also contribute to landslide triggering through rapid snowmelt and excess runoff that occurs during  
493 storms with high heat flux, which can be approximated as the product of mean daily temperature and wind speed (Hasebe and  
494 Kumekawa, 1995). Recent analyses of atmospheric rivers have shown that these storms tend to be responsible for extreme  
495 wind, as well as intense rainfall, and approximately half of the top 2% of wind speed events are associated with atmospheric  
496 rivers (Waliser and Guan, 2017). Warm atmospheric rivers in the Sierra Nevada mountains, California, for example, have been  
497 shown to generate a >1 km increase in the snow elevation over several hours, resulting in unanticipated excess discharge,  
498 flooding, and mass movement events (Hatchett, 2018). In 2017, the contribution of extreme wind-driven snowmelt generated  
499 a >35% increase in stream input to the Oroville Reservoir and the excess runoff resulted in overtopping flows and substantial  
500 (>\$1 billion) damage to the Oroville Dam as well as thousands of downstream evacuations (Henn et al., 2020). For the MP11.2  
501 landslide, the abrupt rise in temperature and high winds on November 20 combined with the rapid disappearance of higher  
502 elevation snowpack imply that wind-driven snowmelt may have contributed to the slope failure by generating excess runoff  
503 and saturation of the initiation zone and downstream colluvial wedges. Most generally, the hydrologic status of colluvial  
504 materials that were destabilized during the MP11.2 event evolved with the combined contributions of antecedent moisture,  
505 rainfall, and snowmelt, although the relative importance of these three sources is unclear.

506 Our field observations of active seepage localized in the SE corner of the MP11.2 head scarp connected to a broad and gentle  
507 ridgeline wetland suggests that the extent and character of terrain above steep slopes constitute a key control on landslide  
508 susceptibility. Our mapping of hydrologic flowpaths along the ridgeline is consistent with these observations and implies that

509 subtle topographic variability may result in significant changes in the upslope or contributing area of landslide-prone slopes.  
510 Similarly, a ponded topographic depression was mapped and monitored upslope of the 2020 Beach Road landslide and narrow  
511 channels directly connected that area to the head scarp (Darrow et al., 2022). The abundance of these broad and gentle high  
512 elevation surfaces (here termed ridgeline water towers) is highly variable across SE Alaska and likely reflects variations in  
513 glacial erosion and bedrock properties (Harris et al., 1974). Combining data from the national wetlands inventory with flow  
514 routing analyses provides an opportunity to identify these ridgeline muskeg (or peatland) drainage systems and characterize  
515 those with potential to influence hydrologic response on landslide-prone slopes. Because peatlands tend to experience rapid  
516 saturation and flashy runoff, they are often sources of storm flow rather than attenuators of high flows (Holden, 2006). As a  
517 result, their potential for contributing to landslide triggering demands investigation. Lidar data is a key requirement for  
518 characterizing surface hydrology in these environments, and active monitoring of the drainage systems would help determine  
519 the magnitude and timescale of hydrologic response and thus the potential contribution to slope instability.

## 520 **5.2 Geologic and geomorphic factors that condition slopes for failure**

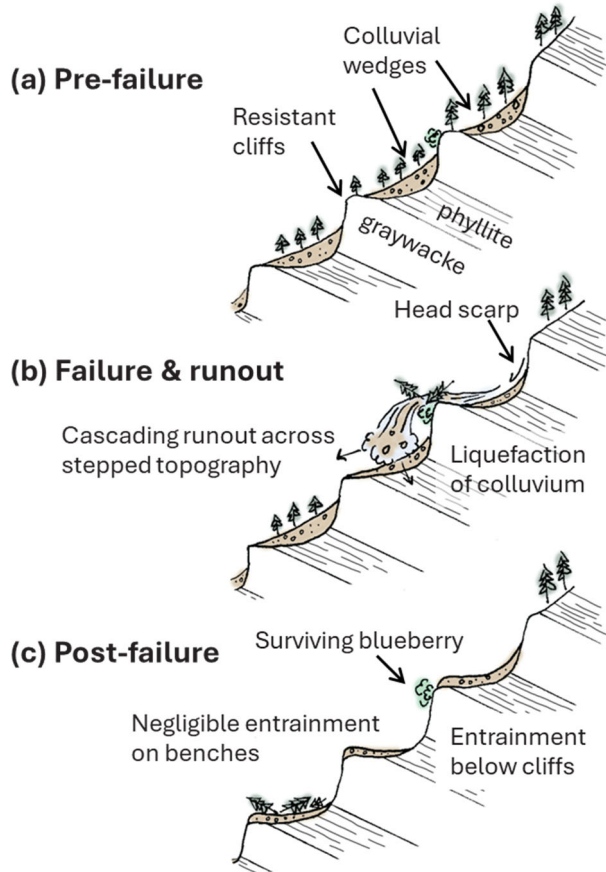
521 An additional factor predisposing the hillslopes above Zimovia Highway to landsliding is the accumulation of thick colluvium  
522 that constitutes the initiation zone of the MP11.2 landslide as well as downslope material that enabled entrainment and  
523 volumetric growth (or bulking) during runout. The thickness of colluvium varies substantially and systematically across the  
524 hillslopes. In the field and from our lidar analyses, we observed extensive colluvial wedges draped below resistant graywacke  
525 layers of the marine sedimentary unit. The punctuated pattern of downslope entrainment highlights how these colluvial wedges  
526 contributed to the volumetric growth and broad area of inundation (Fig. 11d). We interpret these deposits to result from  
527 progressive post-glacial rockfall locally derived from the resistant and underlying sedimentary layers.

528 The combination of east-dipping strata and a west-facing hillslope resulted in the observed pattern of bedrock ledges and thick  
529 colluvial wedges that characterize much of the area, and we surmise that a non-negligible difference in bedrock strength may  
530 be critical for setting up this geomorphic context. Our Schmidt hammer data highlight the high compressive strength of the  
531 graywacke and weak strength of the fine-grained inner beds. At a quarry located just north of the landslide, we documented  
532 bedrock structure and observed active slaking of the fine-grained inner beds that may destabilize the overlying resistant beds  
533 (supplementary materials). Our kinematic analysis showing favourable conditions for flexural toppling is consistent with our  
534 interpretation that progressive failure and retreat of the resistant ledges generate a wake of thick colluvium along the hillslopes  
535 (Imaizumi et al., 2015). Importantly, these colluvial wedges will continue to form and thicken with on-going rockfall along  
536 the resistant cliffs (Moore et al., 2009) although the pace and frequency of this process is unclear. In nearly all cases, the  
537 colluvium is contained within the next downslope bench, which may provide a constraint on the pace of post-glacial bedrock  
538 ledge failure and colluvium production. Examination of the TNFLI revealed dozens of other events on Wrangell Island that  
539 occurred within a similar geomorphic context. Thus, changes in the bedrock dip and resistance, and slope orientation appear  
540 to have a profound effect on the extent and thickness of the colluvial wedges that fuelled the MP11.2 landslide, although  
541 further investigation is beyond the scope of this contribution.

542 **5.3 Controls on landslide runout and volumetric growth**

543 The large volume and extensive inundation area of the MP11.2 landslide likely originated from a thick and wide initiation  
544 zone combined with the entrainment of abundant, saturated colluvium stored on downslope bedrock benches. In this area of  
545 SE Alaska, post-glacial isostatic adjustment forms a fringe of uplifted, low-gradient terrain that may provide a key control on  
546 landslide runout and deposition. In essence, many landslides on Wrangell and nearby islands appear to terminate upon reaching  
547 this low-gradient terrain, when present. Exceptions include particularly large landslides, such as MP11.2, and slides that find  
548 and follow confined flowpaths and behave as channelized debris flows. The MP11.2 landslide's depositional slope of 2° is  
549 substantially lower than values observed on Prince of Wales and Baranof Islands that vary from 4° to 19° and 6° to 26°,  
550 respectively (Booth et al., 2020; Johnson et al., 2000). Given that the mobility value ( $H/L \sim 0.45$ ) for the MP11.2 slide is not  
551 anomalous (Fig. 7a), we interpret its low deposit angle, and thus outsized and tragic impact, to result from highly efficient  
552 entrainment and volumetric growth, which resulted in a large volume and inundation area. Experimental and theoretical  
553 investigations of debris flow runout emphasize that pore pressures generated as wet bed sediment is overridden and  
554 progressively entrained, can reduce friction and facilitate increases in flow momentum (Iverson et al., 2011; Reid, 2011). These  
555 studies emphasize that local slope and volumetric water content are highly sensitive factors that determine the extent of  
556 entrainment during landslide runout (Iverson and Ouyang, 2015). Furthermore, because the colluvial stores on the slope were  
557 emplaced by rockfall activity and soil transport, they may exist in a contractive state such that deformation and shearing  
558 facilitate pore pressure development and volumetric growth.

559



560 **Figure 14.** Schematic of (a) pre-, (b) syn-, and (c) post-slide hillslope geometry, highlighting the influence of resistant bedrock  
 561 and the downslope accumulation of colluvium that becomes mobilized during the landslide event. The live blueberry bush  
 562 below a resistant bed reveals cascading, projectile-like behaviour of the slide material.

563

564 The volumetric growth factor of  $62 \text{ m}^3 \text{ m}^{-1}$  is nearly 10x higher than typical values in unglaciated terrain (Reid et al., 2016),  
 565 highlighting the importance of unconsolidated sediment thickness on steep slopes for determining landslide volume. From a  
 566 mechanistic standpoint, the sequence of subvertical bedrock cliffs along the slide path also suggests that dynamic loading of  
 567 stored colluvium from falling debris may have led to undrained loading and liquefaction (Collins and Reid, 2020). Thus, in  
 568 contrast to check dams that are intended to attenuate momentum of flows in mountain channels (Remaître et al., 2008), the  
 569 sequence of steps in the MP11.2 runout path may have instead facilitated momentum increases through a series of loading-  
 570 induced liquefaction events (Fig. 14). This behaviour has been noted in other highly-mobile landslides with extensive  
 571 inundation zones (Iverson et al., 2015). Lastly, the  $15^\circ$  slope angle that governs the transition between erosion and deposition  
 572 along the MP11.2 landslide is steeper than values observed in unglaciated terrain that features valley confinement and thus

573 enables long runout debris flows (Reid et al., 2016). Acquiring estimates of this transition slope is important for implementing  
574 landslide runout models, such as Laharz and GrfinTools (Brien et al., 2025) and will advance our ability to predict landslide  
575 impacts in the region.

576 **6 Conceptual framework and research needs for shallow landslide assessment in SE Alaska**

577 Our analysis highlights key factors that govern the behaviour and hazard potential of shallow landslides in post-glacial  
578 stepplands, such as SE Alaska.

579 • First, the accumulation of colluvium (or soil) on steep hillslopes serves as a key conditioning process for slope  
580 instability. Previous studies in SE Alaska indicate typical landslide depths of 0.5 to 2.0 m and invoke in-situ  
581 weathering of glacial till, soil creep, and tephra deposition as processes that generate material of sufficient thickness  
582 to initiate shallow landslides (Swanson, 1970). Here, we identify deposition of thick colluvial wedges below resistant  
583 bedrock cliffs as an additional contributor, although the relative importance of these processes remains unclear. More  
584 generally, the timescale of processes that generate colluvium dictates the frequency, magnitude, and spatial pattern  
585 of landsliding in post-glacial landscapes although relevant data are limited.

586 • Second, characterizing water sources and flow accumulation above landslide-prone hillslopes will facilitate the  
587 identification of terrain with high hazard potential. Many glaciated mountains feature broad, gentle ridgetops that can  
588 store and convey large quantities of surface and near-surface water, particularly during snowmelt and rain-on-snow  
589 events. In British Columbia, this terrain is termed “gentle-over-steep” (Jordan, 2016) and efforts to characterize and  
590 map these particular landforms and quantify drainage patterns using airborne lidar data should be a research priority  
591 in SE Alaska.

592 • Third, the runout of debris flows and debris avalanches in SE Alaska is seldom facilitated by channels or  
593 topographic confinement. Rather, most landslides navigate poorly-dissected, post-glacial terrain, and the prediction  
594 of debris flow runout in these settings is challenging owing to highly-variable resistance in the form of vegetation and  
595 flow materials. In these post-glacial settings, the parameters for empirical models (such as the erosion-deposition  
596 transition angle) have not been constrained and the ability of these models to account for controls on runout is  
597 untested. Physically-based models that account for how large wood and variable grain size dictate flow behaviour  
598 also merit further investigation in conjunction with landslide inventory data and field observations.

599 • Fourth, because debris flow volume is the primary control on inundation area, quantification of entrainment along  
600 slide paths is essential for runout modelling. The availability of colluvium and its relative saturation can promote  
601 entrainment. Spatial and temporal variations in these two factors likely depend on the pace and pattern of post-glacial  
602 landscape evolution that determines where colluvium accumulates and how hillslope drainage paths are organized.  
603 Thus, landscape evolution models that are developed and tested in postglacial settings should be a research priority.

604     ● Lastly, although atmospheric rivers have been responsible for all the recent fatal landslide events in SE Alaska, the  
605     character and relative magnitude of these ARs have been highly variable. Some have been notable for producing  
606     several hours of intense rainfall while others have been characterized by protracted rain-on-snow. Thus, quantifying  
607     how the sequencing and character of ARs affects landslide susceptibility will be a key component of efforts to build  
608     a landslide warning system (Nash et al., 2024). Currently, the region lacks sufficient weather station observations and  
609     climate reanalysis productions (Lader et al., 2020) are limited in scope and resolution.

610     Most generally, advancing our understanding of how these geomorphic and atmospheric processes contribute to slope  
611     instability across SE Alaska will inform how we assess, plan, mitigate, and manage landslide hazards and minimize impacts  
612     on public safety and infrastructure.

## 613     **7 Conclusions**

614     The 2023 Wrangell Island landslide was among the most impactful and deadly in Southeast Alaska's recent history and reveals  
615     critical insights into shallow landslide processes in post-glacial terrain. Our investigation demonstrates how geological  
616     structure, post-glacial landscape evolution, hydrologic connectivity, and atmospheric forcing combined to produce a high-  
617     impact event with devastating consequences. Although rainfall intensity during the triggering storm was relatively modest, the  
618     landslide magnitude and impact were amplified by several preconditioning factors that are poorly represented with existing  
619     conceptual models and hazard frameworks.

620     Our key findings include the following:

- 621         ● Evidence of windthrow contributing to the slope failure is lacking, but rain-on-snow dynamics facilitated by high  
622         wind and warm air temperatures may have delivered critical runoff not captured by typical rainfall intensity  
623         metrics.
- 624         ● Ridgetop wetlands with subtle drainage divides control hydrologic routing to many landslide-prone slopes,  
625         concentrating surface flowpaths and downslope slope saturation.
- 626         ● Thick colluvial wedges, perched below resistant bedrock ledges, provided an abundant source zone of readily  
627         mobilized material that fuelled entrainment and long runout.
- 628         ● The transition between erosion and deposition along the stepped flowpath occurred at 15° regardless of position  
629         along the transect, reflecting the profound influence of local slope angle on sediment entrainment.
- 630         ● Stepped topography acted to maintain flow momentum, enabling progressive entrainment and promoting  
631         mobility.
- 632         ● Sequential lidar and flow modelling are essential tools for identifying landslide initiation susceptibility,  
633         erosion/deposition patterns, and geomorphic preconditioning.
- 634         ● Large, high mobility shallow landslides can occur on anti-dip hillslopes and risk may be greater than previously  
635         recognized.

636 These findings highlight high key knowledge gaps and can guide future risk mitigation and early warning strategies in steep,  
637 post-glacial landscapes. Specifically, advancing landslide prediction in SE Alaska requires expanded lidar coverage, integrated  
638 snow and rainfall monitoring, climate modelling, and advances in the modelling of post-glacial landscape evolution,  
639 weathering, and colluvium thickness that provide the means for landslide initiation and entrainment.

640 **Author contributions**

641 MD wrote the proposal and planned the campaign; MD, JR, AP, and AJ performed the fieldwork; MD collected and analysed  
642 the soil and tree samples; JR performed the topographic, climate, and inventory analyses; JR wrote the manuscript draft; MD,  
643 JR, AP, and AJ reviewed and edited the manuscript; AP and MD contributed figures and analyses.

644 **Acknowledgments**

645 The authors thank the National Science Foundation (RAPID EAR Award 2421234 to University of Alaska-Fairbanks) for  
646 supporting this work, Wrangell Cooperative Association for partnership and knowledge sharing, City of Wrangell staff for  
647 resources, discussions, and maps, S. and G. Helgesen for access, A. Park and A. Edwards for fieldwork contributions, A.  
648 O'Brien and T. Belback for sawyer services, Nolan Center staff for hosting multiple community events, and M. Sanders, M.  
649 Reid, D. Staley, K. Barnhart, T. Eckhoff, K. Prussian, J. Foss, S. McKay, J. Montigny, and T. Wetor for insightful  
650 conversations.

651 **References**

652 Alaska Department of Transportation and Public Facilities: Alaska Test Methods Manual: ADOT&PF, 2023.

653 American Society for Testing Materials: Standard Test Method for Determination of Rock Hardness by Rebound Hammer  
654 Method, 2014a.

655 American Society for Testing Materials: Standard Test Methods for Specific Gravity of Soil Solids by Water Pycnometer,  
656 2014b.

657 American Society for Testing Materials: Standard Practice for Classification of Soils for Engineering Purposes (Unified Soil  
658 Classification System), 2017a.

659 American Society for Testing Materials: Standard Test Methods for Particle-Size Distribution (Gradation) of Soils Using Sieve  
660 Analysis, 2017b.

661 American Society for Testing Materials: Standard Test Method for Particle-Size Distribution (Gradation) of Fine-Grained  
662 Soils Using the Sedimentation (Hydrometer) Analysis, 2021.

663 Aydin, A. and Basu, A.: The Schmidt hammer in rock material characterization, *Engineering Geology*, 81, 1–14,  
664 <https://doi.org/10.1016/j.enggeo.2005.06.006>, 2005.

665 Baichtal, J. F., Lesnek, A. J., Carlson, R. J., Schmuck, N. S., Smith, J. L., Landwehr, D. J., and Briner, J. P.: Late Pleistocene  
666 and early Holocene sea-level history and glacial retreat interpreted from shell-bearing marine deposits of southeastern Alaska,  
667 USA, *Geosphere*, 17, 1590–1615, <https://doi.org/10.1130/GES02359.1>, 2021.

668 Benda, L. and Dunne, T.: Stochastic forcing of sediment supply to channel networks from landsliding and debris flow, *Water  
669 Resources Research*, 33, 2849–2863, <https://doi.org/10.1029/97WR02388>, 1997.

670 Booth, A. M., Sifford, C., Vascik, B., Siebert, C., and Buma, B.: Large wood inhibits debris flow runout in forested southeast  
671 Alaska, *Earth Surface Processes and Landforms*, n/a, <https://doi.org/10.1002/esp.4830>, 2020.

672 Booth, A. M., Buma, B., and Nagorski, S.: Effects of Landslides on Terrestrial Carbon Stocks With a Coupled Geomorphic-  
673 Biologic Model: Southeast Alaska, United States, *Journal of Geophysical Research: Biogeosciences*, 128, e2022JG007297,  
674 <https://doi.org/10.1029/2022JG007297>, 2023.

675 Bovy, B., Braun, J., and Demoulin, A.: A new numerical framework for simulating the control of weather and climate on the  
676 evolution of soil-mantled hillslopes, *Geomorphology*, 263, 99–112, <https://doi.org/10.1016/j.geomorph.2016.03.016>, 2016.

677 Brardinoni, F. and Hassan, M. A.: Glacial erosion, evolution of river long profiles, and the organization of process domains in  
678 mountain drainage basins of coastal British Columbia, *Journal of Geophysical Research*, 111,  
679 <https://doi.org/10.1029/2005JF000358>, 2006.

680 Brardinoni, F., Hassan, M. A., Rollerson, T., and Maynard, D.: Colluvial sediment dynamics in mountain drainage basins,  
681 *Earth and Planetary Science Letters*, 284, 310–319, <https://doi.org/10.1016/j.epsl.2009.05.002>, 2009.

682 Brardinoni, F., Picotti, V., Maraio, S., Bruno, P. P., Cucato, M., Morelli, C., and Mair, V.: Postglacial evolution of a formerly  
683 glaciated valley: Reconstructing sediment supply, fan building, and confluence effects at the millennial time scale, *GSA  
684 Bulletin*, 130, 1457–1473, <https://doi.org/10.1130/B31924.1>, 2018.

685 Brien, D. L., Reid, M. E., Cronkite-Ratcliff, C., and Perkins, J. P.: Topographic controls on landslide mobility: modeling  
686 hurricane-induced landslide runout and debris-flow inundation in Puerto Rico, *Natural Hazards and Earth System Sciences*,  
687 25, 1229–1253, <https://doi.org/10.5194/nhess-25-1229-2025>, 2025.

688 Buma, B. and Johnson, A. C.: The role of windstorm exposure and yellow cedar decline on landslide susceptibility in southeast  
689 Alaskan temperate rainforests, *Geomorphology*, 228, 504–511, <https://doi.org/10.1016/j.geomorph.2014.10.014>, 2015.

690 Buma, B. and Pawlik, L.: Post-landslide soil and vegetation recovery in a dry, montane system is slow and patchy, *Ecosphere*,  
691 12, <https://doi.org/10.1002/ecs2.3346>, 2021.

692 Carrara, P. E., Ager, T. A., Baichtal, J. F., and VanSistine, D. P.: Map of glacial limits and possible refugia in the southern  
693 Alexander Archipelago, Alaska, during the late Wisconsin glaciation, *Miscellaneous Field Studies Map*,  
694 <https://doi.org/10.3133/mf2424>, 2003.

695 Cohen, D., Lehmann, P., and Or, D.: Fiber bundle model for multiscale modeling of hydromechanical triggering of shallow  
696 landslides, *Water Resources Research*, 45, <https://doi.org/10.1029/2009WR007889>, 2009.

697 Collins, B. D. and Reid, M. E.: Enhanced landslide mobility by basal liquefaction: The 2014 State Route 530 (Oso),  
698 Washington, landslide, *GSA Bulletin*, 132, 451–476, <https://doi.org/10.1130/B35146.1>, 2020.

699 Cordeira, J. M., Stock, J., Dettinger, M. D., Young, A. M., Kalansky, J. F., and Ralph, F. M.: A 142-year Climatology of  
700 Northern California Landslides and Atmospheric Rivers, *Bulletin of the American Meteorological Society*, BAMS-D-18-  
701 0158.1, <https://doi.org/10.1175/BAMS-D-18-0158.1>, 2019.

702 Darrow, M. M., Nelson, V. A., Grilliot, M., Wartman, J., Jacobs, A., Baichtal, J. F., and Buxton, C.: Geomorphology and  
703 initiation mechanisms of the 2020 Haines, Alaska landslide, *Landslides*, <https://doi.org/10.1007/s10346-022-01899-3>, 2022.

704 DiBiase, R. A., Lamb, M. P., Ganti, V., and Booth, A. M.: Slope, grain size, and roughness controls on dry sediment transport  
705 and storage on steep hillslopes: PARTICLE TRANSPORT ON STEEP HILLSLOPES, *Journal of Geophysical Research: Earth Surface*, 122, 941–960, <https://doi.org/10.1002/2016JF003970>, 2017.

707 Dietrich, W. E., Wilson, C. J., and Reneau, S. L.: Hollows, colluvium, and landslides in soil-mantled landscapes, in: *Hillslope Processes*, edited by: Abrahams, A. D., Routledge, 362–388, <https://doi.org/10.4324/9781003028840-17>, 1986.

709 Dietrich, W. E., Reiss, R., Hsu, M., and Montgomery, D. R.: A process-based model for colluvial soil depth and shallow  
710 landsliding using digital elevation data, *Hydrological Processes*, 9, 383–400, <https://doi.org/10.1002/hyp.3360090311>, 1995.

711 D’Odorico, P. and Fagherazzi, S.: A probabilistic model of rainfall-triggered shallow landslides in hollows: A long-term  
712 analysis, *Water Resources Research*, 39, <https://doi.org/10.1029/2002WR001595>, 2003.

713 Fan, L., Lehmann, P., Zheng, C., and Or, D.: Rainfall Intensity Temporal Patterns Affect Shallow Landslide Triggering and  
714 Hazard Evolution, *Geophysical Research Letters*, 47, e2019GL085994, <https://doi.org/10.1029/2019GL085994>, 2020.

715 Flagstad, L., Steer, A., Boucher, T., Aisu, M., and Lema, P.: Wetlands across Alaska: Statewide wetland map and Assessment  
716 of rare wetland ecosystems, 2018.

717 Gabet, E. J. and Mudd, S. M.: The mobilization of debris flows from shallow landslides, *Geomorphology*, 74, 207–218,  
718 <https://doi.org/10.1016/j.geomorph.2005.08.013>, 2006.

719 Godt, J. W., Wood, N. J., Pennaz, A. B., Dacey, C. M., Mirus, B. B., Schaefer, L. N., and Slaughter, S. L.: National strategy  
720 for landslide loss reduction, *Open-File Report*, U.S. Geological Survey, <https://doi.org/10.3133/ofr20221075>, 2022.

721 Goetz, J. N., Guthrie, R. H., and Brenning, A.: Forest harvesting is associated with increased landslide activity during an  
722 extreme rainstorm on Vancouver Island, Canada, *Natural Hazards and Earth System Sciences*, 15, 1311–1330,  
723 <https://doi.org/10.5194/nhess-15-1311-2015>, 2015.

724 Gonzalez de Vallejo, L. and Ferrer, M.: *Geological Engineering*, CRC Press, London, 700 pp., <https://doi.org/10.1201/b11745>,  
725 2011.

726 Gorr, A. N., McGuire, L. A., Youberg, A. M., and Rengers, F. K.: A progressive flow-routing model for rapid assessment of  
727 debris-flow inundation, *Landslides*, 19, 2055–2073, <https://doi.org/10.1007/s10346-022-01890-y>, 2022.

728 Guan, B., Waliser, D. E., Ralph, F. M., Fetzer, E. J., and Neiman, P. J.: Hydrometeorological characteristics of rain-on-snow  
729 events associated with atmospheric rivers, *Geophysical Research Letters*, 43, 2964–2973,  
730 <https://doi.org/10.1002/2016GL067978>, 2016.

731 Guilinger, J. J., Foufoula-Georgiou, E., Gray, A. B., Randerson, J. T., Smyth, P., Barth, N. C., and Goulden, M. L.: Predicting  
732 Postfire Sediment Yields of Small Steep Catchments Using Airborne Lidar Differencing, *Geophysical Research Letters*, 50,  
733 e2023GL104626, <https://doi.org/10.1029/2023GL104626>, 2023.

734 Guthrie, R. H.: The effects of logging on frequency and distribution of landslides in three watersheds on Vancouver Island,  
735 British Columbia, *Geomorphology*, 43, 273–292, [https://doi.org/10.1016/S0169-555X\(01\)00138-6](https://doi.org/10.1016/S0169-555X(01)00138-6), 2002.

736 Guthrie, R. H., Mitchell, S. J., Lanquaye-Opoku, N., and Evans, S. G.: Extreme weather and landslide initiation in coastal  
737 British Columbia, *Quarterly Journal of Engineering Geology and Hydrogeology*, 43, 417–428, <https://doi.org/10.1144/1470-9236/08-119>, 2010.

739 Haeussler, P. J.: Structural evolution of an arc-basin: The Gravina Belt in central southeastern Alaska, *Tectonics*, 11, 1245–  
740 1265, <https://doi.org/10.1029/92TC01107>, 1992.

741 Hales, T. C.: Modelling biome-scale root reinforcement and slope stability, *Earth Surface Processes and Landforms*, 43, 2157–  
742 2166, <https://doi.org/10.1002/esp.4381>, 2018.

743 Hamilton, T. D.: Late Cenozoic glaciation of Alaska, in: *The Geology of Alaska*, vol. G-1, edited by: Plafker, G. and Berg, H.  
744 C., Geological Society of America, 0, <https://doi.org/10.1130/DNAG-GNA-G1.813>, 1994.

745 Harris, A. S. and Farr, W. A.: The forest ecosystem of southeast Alaska: 7. Forest ecology and timber management., Gen.  
746 Tech. Rep. PNW-GTR-025. Portland, OR: U.S. Department of Agriculture, Forest Service, Pacific Northwest Research  
747 Station. 116 p, 025, 1974.

748 Harris, A. S., Hutchison, K., Meehan, W. R., Swanston, D. N., Helmers, A. E., Hendee, J. C., and Collins, T. M.: *THE FOREST  
749 ECOSYSTEM OF SOUTHEAST ALASKA I. The Setting*, USDA, Portland, OR, 1974.

750 Hasebe, M. and Kumekawa, T.: Estimation of snowmelt volume using air temperature and wind speed, *Environment  
751 International*, 21, 497–500, [https://doi.org/10.1016/0160-4120\(95\)00048-P](https://doi.org/10.1016/0160-4120(95)00048-P), 1995.

752 Hatchett, B. J.: Snow Level Characteristics and Impacts of a Spring Typhoon-Originating Atmospheric River in the Sierra  
753 Nevada, USA, *Atmosphere*, 9, 233, <https://doi.org/10.3390/atmos9060233>, 2018.

754 Hees, W. W. S. van and Mead, B. R.: Extensive, strategic assessment of southeast Alaska's vegetative resources., *Landscape  
755 and Urban Planning*, 72: 25–48, <https://doi.org/10.1016/j.landurbplan.2004.09.027>, 2005.

756 Henn, B., Musselman, K. N., Lestak, L., Ralph, F. M., and Molotch, N. P.: Extreme Runoff Generation From Atmospheric  
757 River Driven Snowmelt During the 2017 Oroville Dam Spillways Incident, *Geophysical Research Letters*, 47,  
758 e2020GL088189, <https://doi.org/10.1029/2020GL088189>, 2020.

759 Holden, J.: Chapter 14 Peatland hydrology, in: *Developments in Earth Surface Processes*, vol. 9, edited by: Martini, I. P.,  
760 Martínez Cortizas, A., and Chesworth, W., Elsevier, 319–346, [https://doi.org/10.1016/S0928-2025\(06\)09014-6](https://doi.org/10.1016/S0928-2025(06)09014-6), 2006.

761 Hovius, N., Stark, C. P., and Allen, P. A.: Sediment flux from a mountain belt derived by landslide mapping, *Geology*, 25,  
762 231, [https://doi.org/10.1130/0091-7613\(1997\)025%253C0231:SFFAMB%253E2.3.CO;2](https://doi.org/10.1130/0091-7613(1997)025%253C0231:SFFAMB%253E2.3.CO;2), 1997.

763 Howe, M., Graham, E. E., and Nelson, K. N.: Defoliator outbreaks track with warming across the Pacific coastal temperate  
764 rainforest of North America, *Ecography*, 2024, e07370, <https://doi.org/10.1111/ecog.07370>, 2024.

765 Imaizumi, F., Nishii, R., Murakami, W., and Daimaru, H.: Parallel retreat of rock slopes underlain by alternation of strata,  
766 *Geomorphology*, 238, 27–36, <https://doi.org/10.1016/j.geomorph.2015.02.030>, 2015.

767 Iverson, R. M.: Landslide triggering by rain infiltration, *Water Resour. Res.*, 36, 1897–1910,  
768 <https://doi.org/10.1029/2000WR900090>, 2000.

769 Iverson, R. M. and Ouyang, C.: Entrainment of bed material by Earth-surface mass flows: Review and reformulation of depth-  
770 integrated theory: Entrainment of bed material, *Reviews of Geophysics*, 53, 27–58, <https://doi.org/10.1002/2013RG000447>,  
771 2015.

772 Iverson, R. M., Reid, M. E., Logan, M., LaHusen, R. G., Godt, J. W., and Griswold, J. P.: Positive feedback and momentum  
773 growth during debris-flow entrainment of wet bed sediment, *Nature Geosci*, 4, 116–121, <https://doi.org/10.1038/ngeo1040>,  
774 2011.

775 Iverson, R. M., George, D. L., Allstadt, K., Reid, M. E., Collins, B. D., Vallance, J. W., Schilling, S. P., Godt, J. W., Cannon,  
776 C. M., Magirl, C. S., Baum, R. L., Coe, J. A., Schulz, W. H., and Bower, J. B.: Landslide mobility and hazards: implications  
777 of the 2014 Oso disaster, *Earth and Planetary Science Letters*, 412, 197–208, <https://doi.org/10.1016/j.epsl.2014.12.020>, 2015.

778 Jackson, R. B., Canadell, J., Ehleringer, J. R., Mooney, H. A., Sala, O. E., and Schulze, E. D.: A global analysis of root  
779 distributions for terrestrial biomes, *Oecologia*, 108, 389–411, <https://doi.org/10.1007/BF00333714>, 1996.

780 Johnson, A. C., Swanston, D. N., and McGee, K. E.: Landslide initiation, runout, and deposition within clearcuts and old-  
781 growth forests of Alaska, *J American Water Resour Assoc*, 36, 17–30, <https://doi.org/10.1111/j.1752-1688.2000.tb04245.x>,  
782 2000.

783 Jordan, P.: Post-wildfire debris flows in southern British Columbia, Canada, *Int. J. Wildland Fire*, 25, 322,  
784 <https://doi.org/10.1071/WF14070>, 2016.

785 Karl, S. M., Haeussler, P. J., and Mccafferty, A. E.: Reconnaissance Geologic Map of the Duncan Canal/Zarembo Island Area,  
786 Southeastern Alaska, Reston, VA, 1999.

787 Korup, O., Densmore, A. L., and Schlunegger, F.: The role of landslides in mountain range evolution, *Geomorphology*, 120,  
788 77–90, <https://doi.org/10.1016/j.geomorph.2009.09.017>, 2010.

789 Lader, R., Bidlack, A., Walsh, J. E., Bhatt, U. S., and Bieniek, P. A.: Dynamical Downscaling for Southeast Alaska: Historical  
790 Climate and Future Projections, <https://doi.org/10.1175/JAMC-D-20-0076.1>, 2020.

791 Lamb, M. P., Scheingross, J. S., Amidon, W. H., Swanson, E., and Limaye, A.: A model for fire-induced sediment yield by  
792 dry ravel in steep landscapes, *Journal of Geophysical Research*, 116, <https://doi.org/10.1029/2010JF001878>, 2011.

793 Lancaster, S. T., Hayes, S. K., and Grant, G. E.: Effects of wood on debris flow runout in small mountain watersheds:  
794 EFFECTS OF WOOD ON DEBRIS FLOW RUNOUT, *Water Resources Research*, 39,  
795 <https://doi.org/10.1029/2001WR001227>, 2003.

796 Larsen, I. J., Montgomery, D. R., and Korup, O.: Landslide erosion controlled by hillslope material, *Nature Geoscience*, 3,  
797 247–251, <https://doi.org/10.1038/ngeo776>, 2010.

798 Lempert, R. J., Busch, L., Brown, R., Patton, A., Turner, S., Schmidt, J., and Young, T.: Community-Level, Participatory Co-  
799 Design for Landslide Warning with Implications for Climate Services, *Sustainability*, 15, 4294,  
800 <https://doi.org/10.3390/su15054294>, 2023.

801 Lin, Y.-C., Hsieh, J.-Y., Shih, H.-S., and Wang, W.-H.: Strong wind is one of the important factors that trigger landslides, *npj  
802 Nat. Hazards*, 2, 12, <https://doi.org/10.1038/s44304-025-00062-x>, 2025.

803 Mann, D. H. and Hamilton, T. D.: Late Pleistocene and Holocene paleoenvironments of the North Pacific coast, *Quaternary  
804 Science Reviews*, 14, 449–471, [https://doi.org/10.1016/0277-3791\(95\)00016-I](https://doi.org/10.1016/0277-3791(95)00016-I), 1995.

805 Marra, F., Armon, M., and Morin, E.: Coastal and orographic effects on extreme precipitation revealed by weather radar  
806 observations, *Hydrology and Earth System Sciences*, 26, 1439–1458, <https://doi.org/10.5194/hess-26-1439-2022>, 2022.

807 Menounos, B., Goehring, B. M., Osborn, G., Margold, M., Ward, B., Bond, J., Clarke, G. K. C., Clague, J. J., Lakeman, T.,  
808 Koch, J., Caffee, M. W., Gosse, J., Stroeven, A. P., Seguinot, J., and Heyman, J.: Cordilleran Ice Sheet mass loss preceded  
809 climate reversals near the Pleistocene Termination, *Science*, 358, 781–784, <https://doi.org/10.1126/science.aan3001>, 2017.

810 Montgomery, D. R., Dietrich, W. E., Torres, R., Anderson, S. P., Heffner, J. T., and Loague, K.: Hydrologic response of a  
811 steep, unchanneled valley to natural and applied rainfall, *Water Resour. Res.*, 33, 91–109, <https://doi.org/10.1029/96WR02985>,  
812 1997.

813 Moore, J. R., Sanders, J. W., Dietrich, W. E., and Glaser, S. D.: Influence of rock mass strength on the erosion rate of alpine  
814 cliffs, *Earth Surface Processes and Landforms*, 34, 1339–1352, <https://doi.org/10.1002/esp.1821>, 2009.

815 Nash, D., Rutz, J. J., and Jacobs, A.: Atmospheric Rivers in Southeast Alaska: Meteorological Conditions Associated With  
816 Extreme Precipitation, *Journal of Geophysical Research: Atmospheres*, 129, e2023JD039294,  
817 <https://doi.org/10.1029/2023JD039294>, 2024.

818 National Oceanographic and Atmospheric Administration (NOAA): NOWData – NOAA Online Weather Data, 2024.

819 Neiman, P. J., Ralph, F. M., Wick, G. A., Lundquist, J. D., and Dettinger, M. D.: Meteorological Characteristics and Overland  
820 Precipitation Impacts of Atmospheric Rivers Affecting the West Coast of North America Based on Eight Years of SSM/I  
821 Satellite Observations, *Journal of Hydrometeorology*, 9, 22–47, <https://doi.org/10.1175/2007JHM855.1>, 2008.

822 Nicolazzo, J. A., Wikstrom Jones, K. M., Salisbury, J. B., and Horen, K. C.: Post-landslide elevation changes detected from  
823 multi-temporal lidar surveys of the November 2023 Wrangell, Alaska, landslides, Alaska Division of Geological &  
824 Geophysical Surveys, <https://doi.org/10.14509/31124>, 2024.

825 Oakley, N. S., Lancaster, J. T., Hatchett, B. J., Stock, J., Ralph, F. M., Roj, S., and Lukashov, S.: A 22-Year Climatology of  
826 Cool Season Hourly Precipitation Thresholds Conducive to Shallow Landslides in California, *Earth Interact.*, 22, 1–35,  
827 <https://doi.org/10.1175/EI-D-17-0029.1>, 2018.

828 Parra, E., Mohr, C. H., and Korup, O.: Predicting Patagonian Landslides: Roles of Forest Cover and Wind Speed, *Geophysical  
829 Research Letters*, 48, e2021GL095224, <https://doi.org/10.1029/2021GL095224>, 2021.

830 Patton, A. I., Roering, J. J., and Orland, E.: Debris flow initiation in postglacial terrain: Insights from shallow landslide  
831 initiation models and geomorphic mapping in Southeast Alaska, *Earth Surface Processes and Landforms*, n/a,  
832 <https://doi.org/10.1002/esp.5336>, 2022.

833 Patton, A. I., Luna, L. V., Roering, J. J., Jacobs, A., Korup, O., and Mirus, B. B.: Landslide initiation thresholds in data-sparse  
834 regions: application to landslide early warning criteria in Sitka, Alaska, USA, *Natural Hazards and Earth System Sciences*, 23,  
835 3261–3284, <https://doi.org/10.5194/nhess-23-3261-2023>, 2023.

836 Ralph, F. M., Neiman, P. J., and Wick, G. A.: Satellite and CALJET Aircraft Observations of Atmospheric Rivers over the  
837 Eastern North Pacific Ocean during the Winter of 1997/98, 2004.

838 Reid, M. E.: Entrainment of bed sediment by debris flows : results from large-scale experiments, *Italian Journal of Engineering  
839 Geology and Environment*, 367–374, <https://doi.org/10.4408/IJEGE.2011-03.B-042>, 2011.

840 Reid, M. E., Coe, J. A., and Brien, D. L.: Forecasting inundation from debris flows that grow volumetrically during travel,  
841 with application to the Oregon Coast Range, USA, *Geomorphology*, 273, 396–411,  
842 <https://doi.org/10.1016/j.geomorph.2016.07.039>, 2016.

843 Remaître, A., van Asch, T. W. J., Malet, J.-P., and Maquaire, O.: Influence of check dams on debris-flow run-out intensity,  
844 *Natural Hazards and Earth System Sciences*, 8, 1403–1416, <https://doi.org/10.5194/nhess-8-1403-2008>, 2008.

845 Rengers, F. K., Kean, J. W., Reitman, N. G., Smith, J. B., Coe, J. A., and McGuire, L. A.: The Influence of Frost Weathering  
846 on Debris Flow Sediment Supply in an Alpine Basin, *Journal of Geophysical Research: Earth Surface*, 125, e2019JF005369,  
847 <https://doi.org/10.1029/2019JF005369>, 2020.

848 Rickenmann, D.: Empirical Relationships for Debris Flows, *Natural Hazards*, 19, 47–77,  
849 <https://doi.org/10.1023/A:1008064220727>, 1999.

850 Rulli, M. C., Meneguzzo, F., and Rosso, R.: Wind control of storm-triggered shallow landslides, *Geophysical Research Letters*,  
851 34, <https://doi.org/10.1029/2006GL028613>, 2007.

852 Schmidt, K. M., Roering, J. J., Stock, J. D., Dietrich, W. E., Montgomery, D. R., and Schaub, T.: The variability of root  
853 cohesion as an influence on shallow landslide susceptibility in the Oregon Coast Range, *Canadian Geotechnical Journal*, 38,  
854 995–1024, <https://doi.org/10.1139/cgj-38-5-995>, 2001.

855 Schuster, R. L. and Highland, L. M.: Socioeconomic and environmental impacts of landslides in the Western Hemisphere,  
856 <https://doi.org/10.3133/ofr01276>, 2001.

857 Schwanghart, W. and Scherler, D.: Short Communication: TopoToolbox 2 – MATLAB-based software for topographic  
858 analysis and modeling in Earth surface sciences, *Earth Surface Dynamics*, 2, 1–7, <https://doi.org/10.5194/esurf-2-1-2014>,  
859 2014.

860 Sharma, A. R. and Déry, S. J.: Contribution of Atmospheric Rivers to Annual, Seasonal, and Extreme Precipitation Across  
861 British Columbia and Southeastern Alaska, *J. Geophys. Res. Atmos.*, 125, <https://doi.org/10.1029/2019JD031823>, 2020.

862 Spinola, D., Margerum, A., Zhang, Y., Hesser, R., D’Amore, D., and Portes, R.: Rapid soil formation and carbon accumulation  
863 along a Little Ice Age soil chronosequence in southeast Alaska, *CATENA*, 246, 108460,  
864 <https://doi.org/10.1016/j.catena.2024.108460>, 2024.

865 Stock, J. and Dietrich, W. E.: Valley incision by debris flows: Evidence of a topographic signature: VALLEY INCISION BY  
866 DEBRIS FLOWS, *Water Resources Research*, 39, <https://doi.org/10.1029/2001WR001057>, 2003.

867 Swanson, F. J., Benda, L. E., Duncan, S. H., Grant, G. E., Megahan, W. F., Reid, L. M., and Ziemer, R. R.: Mass failures and  
868 other processes of sediment production in Pacific northwest forest landscapes, Pages 9–38, in: Ernest O. Salo and Terrance W.  
869 Cundy (eds.), *Streamside Management: Forestry and Fishery Interactions*, Proceedings of a Symposium held at University of  
870 Washington, 12–14 February 1986. Contribution no. 57, Institute of Forest Resources, Seattle, Washington., 1987.

871 Swanston, D. N.: Mass Wasting in Coastal Alaska, *USDA Forest Service Research Paper PNW*, 83, 1–15, 1969.

872 Swanston, D. N.: Mechanics of Avalanche in Shallow till soils of SE Alaska, *USDA Forest Service Research Paper PNW*,  
873 103, 1–16, 1970.

874 Swanston, D. N.: Judging Landslide Potential in Glaciated Valleys of Southeastern Alaska, *Explorers Journal*, 214–217, 1973.

875 U.S. Forest Service: Satellite-based Change Detection Southeast Alaska,  
876 <https://usfs.maps.arcgis.com/apps/webappviewer/index.html?id=12e96b1fdd1546448f8ceec6acadc372>, 2025a.

877 U.S. Forest Service: Tongass Landslide Areas: Data.gov, <https://catalog.data.gov/dataset/tongass-landslide-areas-feature-layer>, 2025b.

879 Vascik, B. A., Booth, A. M., Buma, B., and Berti, M.: Estimated Amounts and Rates of Carbon Mobilized by Landsliding in  
880 Old-Growth Temperate Forests of SE Alaska, *JGR Biogeosciences*, 126, <https://doi.org/10.1029/2021JG006321>, 2021.

881 Waliser, D. and Guan, B.: Extreme winds and precipitation during landfall of atmospheric rivers, *Nature Geosci*, 10, 179–183,  
882 <https://doi.org/10.1038/ngeo2894>, 2017.

883 Wendler, G., Galloway, K., and Stuefer, M.: On the climate and climate change of Sitka, Southeast Alaska, *Theor Appl  
884 Climatol*, 126, 27–34, <https://doi.org/10.1007/s00704-015-1542-7>, 2016.

885 Wheeler, J. O. and McFeely, P.: Tectonic assemblage map of the Canadian Cordillera and adjacent parts of the United States  
886 of America, 1991.

887 Wu, T. H., McKinnell III, W. P., and Swanston, D. N.: Strength of tree roots and landslides on Prince of Wales Island, Alaska,  
888 *Can. Geotech. J.*, 16, 19–33, <https://doi.org/10.1139/t79-003>, 1979.

889 Wyllie, D. C. and Mah, C. W.: *Rock Slope Engineering*, 4th ed., Spon, 456 pp., 2004.

890 Zechmann, J. M., Wikstrom Jones, K. M., and Wolken, G. J.: Lidar-derived elevation data for Wrangell Island, Southeast  
891 Alaska, collected July 2023, Alaska Division of Geological & Geophysical Surveys, <https://doi.org/10.14509/31098>, 2023.

892 Zechmann, J. M., Wikstrom Jones, K. M., and Wolken, G. J.: Lidar-derived elevation data for Wrangell Island, Southeast  
893 Alaska, collected November 28-29, 2023, Alaska Division of Geological & Geophysical Surveys,  
894 <https://doi.org/10.14509/31106>, 2024.